Publication Year	2020
Acceptance in OA@INAF	2022-01-18T15:18:39Z
Title	On the Spatial Distribution of Minor Species in Jupiter's Troposphere as Inferred From Juno JIRAM Data
Authors	GRASSI, Davide; ADRIANI, Alberto; MURA, Alessandro; Atreya, SK; Fletcher, LN; et al.
DOI	10.1029/2019JE006206
Handle	http://hdl.handle.net/20.500.12386/31328
Journal	JOURNAL OF GEOPHYSICAL RESEARCH (PLANETS)
Number	125

On the spatial distribution of minor species in Jupiter's troposphere as inferred from Juno JIRAM data

D. Grassi[1], A. Adriani[1], A. Mura[1], S.K. Atreya[2], L.N. Fletcher[3], J.I. Lunine[4], G.S. Orton[5], S. Bolton[6], C. Plainaki[7], G. Sindoni[7], F. Altieri[1], A. Cicchetti[1], B.M. Dinelli[8], G. Filacchione[1], A. Migliorini[1], M.L. Moriconi[9], R. Noschese[1], A. Olivieri[10], G. Piccioni[1], R. Sordini[1], S. Stefani[1], F. Tosi[1], D. Turrini[1]

(1) Istituto di Astrofisica e Planetologia Spaziali, Istituto Nazionale di Astrofisica, Roma, Italy

(2) Department of Climate and Space Sciences and Engineering, Univ. of Michigan, Ann Arbor, Michigan, USA

(3) School of Physics and Astronomy, University of Leicester, UK

(4) Cornell University, Ithaca, New York, USA

(5) Jet Propulsion Laboratory, California Institute of Technology, Pasadena, California, USA

(6) Southwest Research Institute, San Antonio, USA

(7) Agenzia Spaziale Italiana, Roma, Italy

(8) Istituto delle Scienze atmosferiche e del Clima, Consiglio Nazionale delle Ricerche, Bologna, Italy

(9) Istituto delle Scienze atmosferiche e del Clima, Consiglio Nazionale delle Ricerche, Roma, Italy

(10) Agenzia Spaziale Italiana, Matera, Italy

Abstract

The spatial distribution of water, ammonia, phosphine, germane and arsine in the Jupiter's troposphere has been inferred from the JIRAM-Juno data.

Measurements allow us to retrieve the vertically-averaged concentration of gases between ~3-5 bars from infrared-bright spectra. Results were used to create latitudinal profiles.

The water vapor relative humidity varies with latitude from <1% to over 15%. At intermediate latitudes (30°-70°) the water vapor maxima are associated with the location of cyclonic belts, as inferred from mean zonal wind profiles (Porco et al., [2003]). The high-latitude regions (beyond 60°) are drier in the north (mean relative humidity around 2-3%) than the south, where humidity reaches 15% around the pole.

The ammonia volume mixing ratio varies from 1×10^{-4} to 4×10^{-4}. A marked minimum exists around 10°N, while data suggest an increase over the equator. The high-latitude regions are different in the two hemispheres, with a gradual increase in the south and more constant values with latitude in the north.

The phosphine volume mixing ratio varies from 4×10^{-7} to 10×10^{-7}. A marked minimum exists in the North Equatorial Belt. For latitudes poleward 30°S and 30°N, the northern hemisphere appears richer in phosphine, with a decrease toward the pole, while the opposite is observed in the south.

JIRAM data indicate an increase of germane volume mixing ratio from 2×10^{-10} to 8×10^{-10} from both poles to 15°S, with a depletion centered around the equator. Arsine presents the opposite trend, with maximum values of 6×10^{-10} at the two poles and minima below 1×10^{-10} around 20°S.

1. Introduction

The energy transfer in planetary atmospheres of the Solar System at the pressure level of few bars is dominated by convection and air temperature variations with pressure follow an adiabatic profile [Robinson and Catling, 2013]. In the 0.3-0.6 bar range, for a large variety of conditions, optically thick planetary atmospheres become transparent in the thermal infrared region, so that energy transport is by radiative rather than convective processes [e.g.: Wallance and Hobbs, 2006]. If this convective-radiative boundary is overlaid by atmospheric regions where opacity at short wavelengths (notably ultraviolet) is much higher than in the infrared, absorption of solar photons causes a local heating of the atmosphere and a rise of air temperature while moving upward. The location of the resulting air temperature minimum is defined as the *tropopause*. In Jupiter, the tropopause is found around 0.1 bars [Conrath et al., 1998]. The troposphere is the region located below the tropopause and is where convection plays a major role.

The presence of species other than hydrogen and helium in Jupiter's troposphere down to about 10 bars has long been known from spectroscopic and in situ measurements [see the review by Taylor et al., 2004]. The highly reducing nature of the atmosphere means that the most abundant molecules contain large amounts of hydrogen, e.g. CH_4, but only trace amounts of more oxidized forms such as CO are present, typically at the part per billion level.

Despite convection occurring in the troposphere, a large number of factors conspire to make the composition of the atmosphere variable in the vertical direction. Condensation removes, at different levels in the atmosphere, water, hydrogen sulphide and ammonia, creating complex cloud structure [Atreya et al., 1999]. Furthermore, several other non-condensable species (phosphine, germane, arsine, carbon monoxide) are in thermochemical disequilibrium at the pressure and temperature conditions of the troposphere where they are detected. Their presence at these levels is usually interpreted as evidence of strong convection from deep atmosphere where those species are in thermochemical equilibrium. This identification of molecules as disequilibrium species, and the mechanism for their vertical transport, was first recognized for CO by Prinn and Barshay [1977].

The distribution of minor species is therefore an important observational constraint for theoretical models of the vertical (and horizontal) motions [Fletcher et al., 2009], helping to define the boundary conditions for global circulation models [Young et al., 2018]. More intriguingly, the disequilibrium species in the atmospheres of Jupiter and Saturn provide constraints for the kinetic models for estimating the elemental ratio of oxygen to hydrogen [Fegley and Prinn, 1985; Visscher and Fegley, 2005; Wang et al., 2015]. The O/H ratio is an important consideration in Jupiter's formation models, but difficult to derive directly by IR spectroscopy due to the condensation of water vapor.

Spatial variability in the 5-μm emission has been known for decades and has been linked primarily to changes in cloud opacity with latitude [Irwin et al., 2001]. Brightest latitudes at 5-μm are usually associated with visible dark belts (see Rogers [2009] for the nomenclature of belts and zones). Temporal variability of these 5-μm-absorbing aerosols occurs in distinct multi-year cycles [Fletcher 2017, Antuñano et al. 2018], with unknown origins. Despite its sensitivity to cloud opacity, the 5-

μm region is unique for its ability to probe as deep as ~6 bars, because of relatively low collision-induced opacity due of methane and hydrogen above this level.

Large-scale spatial variability in the deep tropospheric gases was indeed suggested by analyses in the 5 μm transparency window on the basis of Cassini VIMS data [Giles et al., 2015] and ground-based observations. For instance, Bjoraker et al., [2015] and Giles et al., [2017a] and Giles et al., [2017b] have reported the latitudinal variations of disequilibrium species, while distribution of ammonia has been detailed by Giles et al., [2017b] and Blain et al., [2018].

These global distributions derived at 5 μm refer to pressure levels of a few bars and are complemented by data in other spectral regions, that allow one to probe nearby altitudes. Namely, latitudinal coverage for phosphine at atmospheric pressures levels slightly less than 1 bar has been achieved using the molecule's 8.5 μm band [Fletcher et al. 2009]. The same is true for ammonia, the latitudinal distribution of which cames from 10 μm studies by Voyager IRIS [Gierasch et al., 1986] and Cassini CIRS and IRTF/TEXES [Achterberg et al., 2006; Fletcher et al., 2016]. A major breakthrough for ammonia has recently been achieved by the measurements of the Juno Microwave Radiometer (*MWR*) that enable an estimate of the abundance of this species from 0.5 bar to tens of bar pressure levels on large longitudinal swaths [Li et al., 2017, Bolton et al. 2017].

Summarizing these efforts, we note here that an equatorial maximum and low latitude (~15° on both hemispheres) minima in ammonia have been seen in the thermal-IR and microwave data, probing the 0.1-0.5 and 0.5-90 bars pressure ranges, respectively. An equatorial maximum in phosphine has been shown in the thermal-IR, probing between 0.5 and 0.9 bars [Fletcher et al., 2009], but not at 5 μm, where data are sensitive to the 4-8 bars region [Giles et al., 2017a]. The latitudinal distributions of AsH_3 and GeH_4 show tantalizing structure, but this has proven very hard to disentangle from aerosols that scatter both thermal photons and reflected sunlight [Giles et al. 2017a].

Considering smaller spatial scales, several authors have previously reported the variability in the mixing ratio of minor species at the level of few bars in the so-called '5-μm hot spots', regions of anomalously high 5-μm emission found at the southern rim of the North Equatorial Belt [Irwin et al., 1998, Grassi et al., 2017a and references therein]. Another example of a geographically limited study was given by Sindoni et al. [2017], where the authors described local variations of ammonia around anticyclonic 'White Ovals' located about 35°S, from measurements by the Jovian Infrared Auroral Mapper (*JIRAM*) on board NASA's Juno spacecraft.

The present paper aims to complement previous studies with an extensive analysis of the spectral measurements performed by JIRAM in the 5-μm windows during the first two years of the Juno mission. Section 2 describes briefly JIRAM and operations. Section 3 summarizes the analysis method, whose details have been published in our previous papers [Grassi et al, 2017a,b]. Uncertainties and possible sources of ambiguity in interpretation are also outlined. Section 4 presents the results of the analysis, detailing inferred spatial variations. In Section 5 we discuss the results, with comparison against previous work and theoretical predictions.

2. Dataset

JIRAM [Adriani et al., 2014] consists of an infrared spectro-imager covering the 1.993-5.014 μm range with an average spectral sampling of 9 nm/band (average spectral resolution of 15 nm). The spectrometer acquires simultaneously 256 spectra, arranged along a line of spatially contiguous pixels (a "slit"). JIRAM spectra are often complemented by context images acquired integrating the incoming radiance over a broad spectral range centered around 4.8 μm (M-filter imager). The field of view of individual pixels (for the spectrometer as well as for the imager) is about 240 μrad. Therefore, the field-of-view of the JIRAM spectrometer consists of an area of 1x256 pixels and covers on the celestial sphere 240 μrad x 3.5° (being 3.5°= 256 x 240 μrad). Hereon, unless otherwise specified, "JIRAM" stands for "JIRAM spectrometer".

Juno is a spinning spacecraft and the JIRAM pointing system has only one degree of freedom, the long direction of the slit being forced to be parallel to the Juno rotation axis. This implies that the slit can be placed arbitrarily over a band in the sky of width 3.5° having the Juno rotation axis as its polar axis. Since JIRAM can acquire only one slit at each Juno spacecraft rotation (2 rpm), gaps or overlaps between slits from consecutive rotations may exist, depending upon timing of measurements. Consecutive slits are in general not spatially connected.

Adriani et al., [2014] described the extensive on-ground spectral, geometric and radiometric calibrations performed on the JIRAM flight model prior to launch. In-flight calibration relies essentially on periodic observations of internal calibration sources (high temperature black bodies and deep space) to characterize and monitor long-term variations of instrument spectral responsivity, thermal background and read-out noise. In-flight calibrations procedures were validated during the 2013 Juno's Earth flyby by means of dedicated observations of the Moon [Adriani et al., 2016].

JIRAM observes Jupiter for short periods of about two days surrounding each Juno perijove passage ("PJ"), which occurs every 53 days, Juno's orbital period. Even during these PJs, Jupiter may often fall outside the 'visibility strip' described above, because of specific spacecraft attitudes and the evolution of Juno's orbit.

The overall result is a relatively sparse spatial coverage, strongly variable from PJ to PJ. In this study, we considered the data acquired in the first two years of Juno operations, i.e. from PJ1 to PJ15 (Aug. 27th 2016 - Sept. 7th 2018). Owing to a spacecraft safe-mode event and its subsequent diagnosis and testing, JIRAM was not operated in PJ2 and PJ3. The coverage achieved in PJ1 has been so far the most complete and is presented in Fig. 1. System III [Archinal et al., 2011] is adopted to provide geographic coordinates, with longitude increasing while moving *west*ward. Planetocentric latitudes are used throughout. The two panels of Fig. 1 present JIRAM coverage achieved during the two planning periods of PJ1, JM0002 (from 2.2 to about 1 day before PJ1) and JM0003 (from 1 day before PJ1 to about one day after PJ1). The distinction is required to avoid the merging of different features due to motion of cloud systems with respect to System III. Coverage maps for other PJs are presented in supplementary materials (figure S1).

JIRAM data used for this analysis are publicly available at the NASA Planetary Data System [Noschese and Adriani, 2017].

3. Methods

In this work we adopted the analysis method for JIRAM data described in Grassi et al., [2017b], and used in Grassi et al., [2017a], which provided context for the analysis of Orton et al., [2017]. Further discussion on the JIRAM data information content was given in Grassi et al., [2010]. Here we summarize the key features of the procedure.

The analysis is limited to the spectral range between 4.08 and 5.01 μm. Despite its scientific interest, the inclusion of the solar-dominated 2-4 μm range would require the treatment of solar photons scattering, with significant computational burden and considerable uncertainties on the forward-modeling errors related to the assumptions of the cloud properties. On the other hand, the 'no solar source' approximation is partly justified by our specific focus on these bright areas (assumed to be relatively depleted in clouds), where the scattered solar contribution in the 4-5 μm region is expected to be between 100 and 800 times smaller than the thermal component, as reported previously by Drossart et al. [1998]. Even for the instances of thickest clouds (more effective reflection) considered in this study, simulations suggest that the scattered solar contribution remains below 3% of the total signal. Free parameters of the spectral fit are (1) the relative humidity of water vapor, the mean mixing ratios of (2) ammonia, (3) phosphine, (4) germane and (5) arsine (which all contribute to the spectral absorption in this spectral region) and (6) the residual opacity of the 1-bar cloud at 5 μm. The retrieval code also includes as formal fit parameters the ammonia relative humidity above its condensation level as well as the phosphine fractional scale height above the 1-bar level. The analysis presented in Grassi et al. [2017b] demonstrated, however, that actual sensitivity to these parameters is compromised by expected levels of forward modeling approximations and therefore they do not significantly vary from their a priori values of 12% and 25% respectively. Therefore, the values of ammonia relative humidity and phosphine fractional scale height are not discussed in this work. The cloud is assumed to be spectrally flat, with a single scattering albedo ω equal to 0.9 and an asymmetry factor g equal to 0.7, consistently with the findings of Giles et al., [2015]. The cloud is assumed to extend between 1.3 and 0.7 bar, with uniform density along altitude in this pressure range and zero elsewhere. The lower and upper limits of the cloud are in agreement with the previous results of Giles et al., [2015] and Drossart et al. [1998], respectively. During retrieval, the analysis code varies the opacity applying, as a free parameter, a scalar multiplicative factor to this uniform density profile. Sources of gaseous spectroscopic data are given in Grassi et al. [2010] and Grassi et al. [2017b]. For germane, it should be noted that line data are not (yet) reported in the reference HITRAN database [Gordon et al., 2016] and the authors have to resort to other databases. While the GEISA dataset [Jacquinet-Husson, N., et al., 1999] had been adopted for several years, its description of different germane isotopes remains largely incomplete. On the other hand, theoretical databases (e.g.: Spherical Top Data System – STDS - Wenger and Champion, [1999]) needed to have their line intensities corrected on the basis of experimental data, until a new completely self-consistent line

list was published by Boudon et al. [2018]. The germane line list used in our work was prepared before the Boudon et al. [2018] publication, on the basis of STDS and experimental data by Schaeffer and Lovejoy [1985]. It turned out to be consistent within 5% with the Boudon et al. [2018] latest update.

Fig. 2 shows examples of spectral fits provided by the retrieval code. We note the systematic radiance excess in model spectra at 4.61 and 4.95 μm and systematic deficiencies at 4.69 and 4.724 μm. It shall be noted that in order to achieve an adequate fit of the data, the theoretical spectral resolution of JIRAM (i.e.: the FWHM of the spectral response function of individual sampling points) considered in the computation of simulated observations was degraded by a factor 1.3. While this is appropriate for most of the JIRAM range at λ>4.4 μm, comparison against other datasets and corresponding best fit models presented by Giles et al. [2017a], Giles et al. [2015], Irwin et al. [1998] and Roos-Serote et al. [1998] suggest that a more accurate description of the JIRAM spectral response function is probably required at most of the misfit positions mentioned above.

Test runs on sets of simulated observations clearly indicate that the main limitation of the retrieval system is represented by the accuracy of the forward modeling subroutine embedded in the analysis code [Grassi et al. 2017b]. This subroutine relies on the correlated-k approach (with 30 quadrature points) for the treatment of gaseous opacities and on the two-stream approximation (as implemented in the TWOSTRM subroutine [Kylling, et al. 1995]) for the treatment of multiple scattering in order to achieve acceptable run times. Its results, once compared against the outcomes of a rigorous treatment (line-by-line coupled with DISORT [Stamnes et al., 1998]) show differences about a factor 10 greater than the JIRAM instrumental Noise Equivalent Radiance (NER), as estimated in Adriani et al. [2016]. This forward-modelling performance, which may appear rather poor, must, however, be evaluated in view of the exceptional JIRAM signal-to-noise ratio, that exceeds 500 in the Hot Spot observations and is well in line with the accuracy better than 5% of the NEMESIS code [Irwin et al., 2008]. Since modeling errors are roughly proportional to the absolute signal, we found it to be more appropriate to quantify the fit quality ("quality parameter") as the average *relative* difference between the best fit (s_{bf}) and the observed (s_{obs}) spectrum over the N JIRAM spectral sampling points j=1, … N in a given range (4.6-5.0 μm in our case)

$$fit\ quality = \sum_{j=1}^{N} \left| \frac{s_{bf,j} - s_{obs,j}}{s_{bf,j}} \right| / N \cdot 100 \quad (1)$$

rather than rely on a χ^2 value

$$\chi^2 = \sum_{j=1}^{N} \left(\frac{s_{bf,j} - s_{obs,j}}{NER_j} \right)^2 / (N - n_{par}) \quad (2)$$

computed on the basis of a fixed NER (n_{par} being in eq. (2) the number of free fit parameters in retrieval).

However, the forward-modeling errors presented in Grassi et al., [2017b, fig 3. there], remain indicative of typical conditions of relatively bright Jupiter spectra and allow one to define an effective noise level - presented in Fig. 2 (red curve) – as the quadratic sum of the NER and of

random and systematic components of forward-modeling errors. Once this effective noise level is considered, the Bayesian formalism [Rodgers, 2000] allows one to estimate the approximate 1-σ uncertainties for the retrieved quantities of different gases from individual spectra as follows: $Log_{10}([H_2O]_{RH})$~0.16, $[NH_3]$~6.7×10^{-5}, $[PH_3]$~6.7×10^{-8}, $[GeH_4]$~1.1×10^{-10}, $[AsH_3]$~1.3×10^{-10} (We anticipate here that water vapor is by far the most variable gas in the Jupiter atmosphere and we found therefore appropriate to retain, for most cases, the logarithm of relative humidity - i.e.: the original state vector element in our retrieval code - rather than convert it to a mixing ratio). These error magnitudes are about ten times higher than those expected on the basis of the solely JIRAM NER. The effects of these 1-σ variations on a bright spectrum (opacity of the residual cloud equal to 0.1) are presented in Fig. 3. In rigorous terms, these errors refer to the neighborhood of the a priori state vector, as defined in Grassi et al., [2017b], Table I there, but are assumed to be roughly representative of the entire dataset.

The degeneracy of the inverse problem (where the spectral effect of an erroneous estimate of a parameter is compensated by an erroneous estimate of another parameter) is difficult to assess in general terms. Nonetheless, one can consider the off-diagonal elements of the *a posteriori* covariance of the solution (S matrix in the nomenclature of Rodgers [2000]). Indeed, these elements provide a clue to the correlations among retrieved values of free parameters (1-6 listed earlier) as induced by degeneracy. Considering again the neighborhood of the a priori state vector, the correlation between the retrieved values of gases is relatively low, being the highest (0.43) between water and arsine and between water and phosphine (0.45). Notably, the gas estimates are usually *positively* correlated, i.e.: possible excesses in the estimate of a gas are compensated by excesses in other gases. Retrieved gas content are *negatively* correlated to the retrieved cloud opacity at the 1-bar level, there being a stronger correlation between opacity and water (-0.54). The actual sensitivity of the retrieval system to free parameters (1) - (6) was further confirmed by a series of specific tests on limited subsets of several hundreds of JIRAM spectra uniformly distributed at different latitudes (see table I in supplementary materials). In each test, a single gas was kept fixed at its a priori value while others were allowed to vary in an attempt to reproduce the data. The quality of the fit (regardless whether estimated by the "quality parameter" or by an effective χ^2 that includes also the forward modeling errors) was eventually compared against those of the reference case (where all parameters are allowed to vary). Paired-samples Student's t-tests (as well as Wilcoxon signed-rank tests, Siegel [1956]) strongly support the view that fit quality is significantly deteriorated by keeping any of (1) - (6) fixed (the null hypothesis 'average of fit difference is zero' always has a probability $p<10^{-6}$).

For all minor gases whose abundances are being retrieved, JIRAM data have a peak sensitivity at about 4.5 bars for regions with an opacity at 5 μm equal to 1 and observed with an emission angle equal to zero [Grassi et al. 2010]. The position of the sensitivity peaks of different gases is expected to move slightly upward with increasing emission angle, while cloud opacities much greater than one essentially push the peak sensitivity region above the nominal 1-bar cloud level.

Sources of systematic errors include assumptions on aerosol properties, such as particle-scattering properties and cloud location. A test performed considering g = 0.8 instead of g = 0.7 induced a minor albeit statistically detectable deterioration of the fit. More interestingly, our retrieval code

does not consider the opacity of a 'deep' 5-bar cloud proposed by Bjoraker et al., [2015] and discussed as a possible scenario also in Giles et al. [2017a]. A specific test on a limited subset of about 1000 spectra was carried out including such a structure in the forward model and its thickness as a free parameter in data modeling. Statistically significant improvements in fit quality were observed only over the South and North Equatorial Belts, where an *increase* of the deep cloud thickness was obtained, a trend opposite to that reported by Giles et al [2017a]. At latitudes higher than 20° (in both hemispheres), the inclusion of the deep cloud leads to a slight deterioration of fit quality (the null hypothesis retains however a probability around 0.13 once estimated with the Student's t-test). Moreover, contrary to what found by Giles et al [2017a], the deep cloud can not modify qualitatively the latitudinal trends described in following section 4.1 (figure S2 in supplementary materials). Giles et al [2017a], forcing a constant value of $[GeH_4] = 0.58 \times 10^{-9}$ (the value they initially retrieved on South Equatorial Belt) over the entire planet and allowing for variations of the opacity of the deep cloud, obtained a fit quality comparable to the one achieved considering the germane content as a free parameter. A similar test on JIRAM data with our retrieval scheme provided a different outcome, with a fit quality clearly inferior in the case of fixed $[GeH_4]$ and variable deep cloud opacity. These ambiguities, along with the limits in our forward modeling subroutine (that would affect in the scattering treatment) suggested that we could omit the 'deep' 5-bar cloud hypothesis in the present analysis. As mentioned before, the radiometric accuracy of JIRAM is such that large margin exists for further refinements of analysis if more accurate forward methods are adopted. Under these conditions, the actual occurrence of a deep cloud can be possibly investigated on firmer ground in future efforts. Table II in supplementary materials summarizes the results of tests on clouds.

Other ambiguities may arise from the adopted state vector (set of parameters to be retrieved), that can - in principle - be oversimplified. Grassi et al. [2010] demonstrated the sensitivity of JIRAM data to vertical *profiles* of phosphine (not just mean mixing ratio) over a vertical range of at least 60 km, well above the typical width of averaging kernels (25 km). Some vertical sensitivity exists also for water and ammonia, albeit over a much more limited pressure range.

A further point to keep in mind is the sensitivity of our results to the vertical temperature vs. pressure profile, which we take from Seiff et al. [1998] on the basis of the Galileo Entry Probe measurements. Numerical tests demonstrate that a systematic increase or decrease of 5K at *every* fixed pressure level of our atmospheric model induces a *relative* variation of about 2% in the retrieved contents of ammonia and phosphine, of 5% in germane and arsine and 15% in water (for water, this shall be interpreted as relative variations on the current value of relative humidity: i.e.: at 15% relative humidity we can vary between 12,75% and 17,25% *not* between 0 and 30%!) Higher sensitivity for water is related to our choice to consider (the logarithm of) relative humidity as a state vector element in our retrieval code and to the high sensitivity of saturation pressure to temperature. In a further test, we replaced the Seiff et al. [1998] profile with the wet adiabat presented by Showman and Ingersoll [1998] (fig. 6c there). The amplitudes of the resulting systematic variations on the retrieved contents remain within the retrieval uncertainties quoted above for each gas, retaining even the smallest details of the latitudinal trends described in section 4.1.

Having clarified the general features of the retrieval code, we shall now describe the specific pre- and post- processing steps adopted in this work.

Retrievals were performed on individual JIRAM spectra (no averaging or similar procedures) and were performed only on a subset of available data. The sub-selection aimed to speed up the analysis of the dataset and to improve the uniformity and quality of the results. More specifically, data were selected on the basis of 1) Radiance at 5 μm / cos (emission angle) > 20 μW/(cm^2 sr μm), corresponding to a brightness temperature of about 237K, to select *a priori* the cases with lower cloud opacity that allow probing of the troposphere to a deeper extent 2) Emission angle < 40°, to limit uncertainties related to modeling of cloud scattering 3) Pixel size < 500 km, to limit variability inside the field-of-view. The constraint on radiance drastically reduces the number of spectra from 1.7×10^6 cases to 4.2×10^5. This constraint introduces also a strongly uneven latitude distribution in the selected population, because of the uneven latitudinal distribution of radiance over the disk of Jupiter as observed in the overall JIRAM dataset (Fig. 4). The analysis of the selection required about three months of computational time on our available facility (six Intel Core i7-7700K CPU @ 4.20GHz, 32Gb RAM).

The resulting retrievals were further filtered *a posteriori*, rejecting cases with 1) poor fit (relative discrepancy > 6%) or 2) high *retrieved* cloud opacity (>2). The 6% threshold was heuristically set considering the distribution of the fit quality parameter (1) over the processed dataset. This distribution shows a clear peak located at 3.6% (comparable to the quality of forward modeling discussed above) and an half-width-at-half-maximum of 0.7%. The final population of state vectors has a size of 3.7×10^5 and is the one considered for the remainder of this article. It must be kept in mind that it refers to the conditions found in infrared-bright, cloud-free regions and not necessarily to Jupiter as a whole.

4. Results

The retrieved gas abundances have been used to study (1) latitudinal profiles, (2) features mapping (for available spatial coverage), and (3) statistical relationship between different gases. Note that comparison against previous literature results on (1) and (2) is given in section 5.1.

4.1 Latitudinal profiles

Retrievals have been classified according to latitude (bin size = 1°) and PJ. For each bin, the mean and standard deviation have been computed. Resulting latitudinal profiles (mean over different longitudes at a fixed latitude) are presented in Figure 5. Panels of Fig. 5 present also the mean profiles as computed separately for different PJs, to provide an idea of the stability of the latitudinal trends over the period encompassed by PJ1 and PJ15. The sharp latitudinal variations occasionally observed on these profiles are usually associated to very small spectrum populations for a given latitude bin, as can be inferred from the coverage maps presented in fig. S1 in Supplementary Materials.

The water vapor relative humidity (Fig. 5a) is by far the most variable parameter amongst the ones retrieved so far. It shows a well-defined pattern of maxima and minima along latitude, varying from < 1% to well above 15% in the southern polar region. For most latitudes, the standard deviation exceeds the mean value, suggesting a strong longitudinal as well as PJ-to-PJ variability. The position of extremes is however fairly constant over different PJ: maxima are found at 68°S (substantial), 52°S, 43°S, 35°S, 15°S and 7°S, 15°N, 26°N, 35°N, 45°N, 52°N. No obvious correlation exists with the pattern of infrared brightness in Fig. 4b: maxima of infrared-brightness are often associated with water vapor minima (e.g: 10°N, in the hot-spot region, 58°N, 12°S and 17°S, 38°S, 74°S), albeit an opposite correlation (max-max) is sometime observed (26°N, 35°N) for weak increases in brightness. More intriguing is the correlation against the wind speed profiles at the top cloud levels described by Porco et al., [2003] (Figure 6). For intermediate latitudes (between 30° and 70° in both hemispheres), the maxima in water vapor occur systematically 3° to 5° poleward of a prograde (eastward) jet and equatorward of the next retrograde (westward) jet found moving toward the pole. The maxima in water vapour corresponds therefore to cyclonic regions, usually associated with visible belts (Ingersoll et al., [2004]). At equatorial latitudes (between 30° and 0°) the correspondence becomes more ambiguous. The water vapor peak at 68°N is located in a retrograde flow that marks the start of polar dynamical domains. Noteworthy is the asymmetry in water vapor of the two hemispheres for latitudes poleward of 55°; the southern hemisphere is much wetter, with the relative humidity increasing from <1% at 55°S to above 15% at 85°S versus an increase from about 1% to 5% observed between 55°N at 85°N. In retrievals, the water relative humidity has an initial value of 10%.

The main feature seen in the ammonia latitudinal profile (Fig. 5b) is a marked increase at both boundaries of the Equatorial Zone (EZ), though the EZ region itself is not covered by retrievals due to its high opacity. A strong depletion (mixing ratio $< 1.5 \times 10^{-4}$) is observed between 10°N and 17°N, without a southern counterpart. At other latitudes, trends are less pronounced. Northward of 25°S, the ammonia mixing ratio is relatively constant around 3×10^{-4}, with a possible slight increase

only above 80°N. In the southern hemisphere, we note a more gradual increase from 2.5×10^{-4} at 20°S to 4×10^{-4} close to the south pole. Along this general southward increase, two local maxima at 68°S and 52°S seem to persist over different PJs. Local maxima were also found for water vapor at the same locations, and they occur poleward of prograde jets and equatorward of retrograde jets. The initial value of ammonia mixing ratio in the retrievals is 2.2×10^{-4}.

The phosphine latitudinal profile (Fig. 5c) has a strong minimum at 10°N (sharper than the nearby ammonia minimum), where it falls below 5×10^{-7}. In the northern hemisphere we observe a very smooth decrease from about 9×10^{-7} at 40°N to 8×10^{-7} at the north pole. In the southern hemisphere values are between 7×10^{-7} and 8×10^{-7} between 15°S and 50°S, increasing to 1×10^{-6} at the south pole. Also for phosphine, a local maximum is observed at 68°S, in a consistent manner over different PJs. The initial value of phosphine mixing ratio in the retrievals is 6×10^{-7}.

Germane (Fig. 5d) shows marked latitudinal trends, despite inherently higher retrieval errors with respect to those of water, ammonia and phosphine (compare panels a, b, c and f of Fig. 3 in Grassi et al., [2010]). Retrievals on both sides of the Equatorial Zone indicate a strong depletion over the equator, while the maximum value (9×10^{-10}) is achieved at 15°S, without a northern hemisphere counterpart. Observed trends at the borders of the North and South Tropical Belts (centered at 25°S and 23°N respectively) are also suggestive of local germane depletions. Poleward of 40° latitude in both hemispheres, germane decreases essentially monotonically, with the decrease being steeper in the south. At both poles the mixing ratio is close to 2×10^{-10}. The initial value of germane mixing ratio in the retrievals is 4.5×10^{-10}.

Arsine (Fig. 5e) also shows a marked latitudinal behavior. The entire region between 50°S and 40°N presents mixing ratios below about 2×10^{-10}, with a significant peak of 3×10^{-10} at 10°N (close to the locations noted for minima in ammonia and phosphine mixing ratios) and a minimum below 1×10^{-10} at 20°S. Poleward of this large latitudinal range, arsine strongly increases toward both poles. In the northern hemisphere, it gradually reaches a value between 5×10^{-10} and 6×10^{-10}, while in the south it abruptly rises from 2×10^{-10} to 6×10^{-10}, from 55°S to 70°S (the same location of water, phosphine and ammonia maxima) remaining constant afterward toward the pole. The initial value of arsine mixing ratio in the retrievals is 2.4×10^{-10}.

A plot of latitudinal trends of retrieved cloud opacity is provided in figure S3 in the supplementary materials. This plot however is severely biased by data filtering described in section 3 and should not be interpreted as representative of the global distribution of opacities in the Jupiter's atmosphere.

The latitudinal trends described in this section are representative of the conditions in IR-bright regions of Jupiter's atmosphere. The main features presented have amplitudes largely exceeding the conservative uncertainties considered for individual spectra, while the dispersion inside each latitude bin (blue thick curves in the panels of Fig. 5) is systematically even smaller than these uncertainties (supporting the view that formal uncertainties stated in section 3 are indeed very conservative). Possible systematic errors are likely to be more significant. As anticipated in section 3, a specific test where a deep 5-bar cloud had been included in the forward model did not alter substantially the latitudinal trends of minor gases (albeit absolute values were modified beyond

their nominal 1-σ error bars). We also mentioned that the removal of any gas from the set of free parameters implies a statistically significant deterioration of fit quality, pointing against a major role of degeneracy in driving the presented trends (if this were the case, degeneracy would have compensated the fit efficiently by altering the remaining free parameters). Moreover, given the expected (moderate) positive correlation between *retrieved* gas contents on the basis of the typical values of solution covariance matrix S discussed in section 3, a *substantial* degeneracy would produce very similar trends for all gases, contrary to what is seen in Fig. 5. There, highest correlation (0.6) is found between ammonia and phosphine, but the minimum in the North Equatorial Belt (the most remarkable feature of their latitudinal trends), is significantly larger for ammonia, arguing again against a major role of degeneracy in driving this feature. Similarly, the latitudinal profile of opacity (see figure S3 in supplementary materials) in our data do not show any specific trend opposite to the gas distributions (again, on the basis of values commonly observed for the S matrix). The highest anti-correlation is observed between opacity and arsine (-0.67), but the decrease of opacity between 25°S and 5°S is not matched by a rise in arsine, nor does the sharp fall of arsine at 68°S have any clear opacity counterpart. The arsine peak at 10°N actually occurs north of a strong opacity minimum and therefore the two features cannot be correlated on the basis of degeneracy. Also noteworthy is the large spread of opacity values at a given latitude, to be compared against the rather uniform values of minor gases (except for water), another point supporting a minor role of degeneracy from opacity in our results. For water vapor, the relationship noted with wind profiles (that are derived from entirely different datasets, Porco et al., [2003]) further supports the view that reported latitudinal trends are indeed genuine features.

4.2 Distribution over discrete longitudinal features

Here we focus on low and intermediate latitude regions. For a more extensive discussion on circumpolar regions (for latitudes above 80° in both hemispheres), the reader is referred to Adriani et al., [2019].

Data from PJ1 (Fig. 1) offers by far the most complete spatial coverage among all available PJs and will be considered exclusively for the following discussion.

Water vapor is highly variable (Fig. 7a-b), as already mentioned in section 4.1. Noteworthy are the longitudinal variations in the North and South Equatorial Belts. Namely, while the hot spots previously described in Grassi et al., 2017a (238.3°W, 8.3°N and 134.4°W, 7.6°N) are indeed relatively dry locations, other longitudes at the same latitudes (best seen in Fig. 7c at 288° W and 312°W, and also in Fig. 7b at 40°W, 95°W, 115°W, 160°W, 210°W and 260°W) are very rich in water vapor (relative humidity > 15%). These spots move eastward during observations of PJ1 (compare Fig. 7a and 7b) with speeds comparable to those reported at this latitude for visible clouds by, e.g., Porco et al., [2003] and Tollesfson et al. [2018]. Other limited “wet” locations are found around latitude 14°N at 325°W, 300°W (Fig. 7c), 115°W (apparently associated with vortices with 5-μm bright central parts) and at latitudes about 7°S, mostly between 90°W and 180°W. The infrared-bright annulus around the Great Red Spot (GRS, 310°W at the time of PJ1, see again Fig. 7c) as well as the entire latitude containing the White Ovals at 40°S are remarkably dry (relative humidity < 2%). Water vapor also shows some local strong enhancements (relative humidity above

15%) beyond 45°N and 50°S. An example from PJ9 is presented in Fig. 7d. As already noted at 14°N, these wet spots often correspond to the interiors of isolated vortices with a well-defined shape that appear, on the basis of the orientation of the arms, cyclonic structures (counterclockwise in the north, clockwise in the south). Correlation with morphology is made difficult by the variable cloud thickness, that in cyclone centers often exceeds values for which retrievals are meaningful. Turbulent areas observed between well-structured vortexes are relatively dry, being wetter in the south (about 10%) than in the north (3%).

The distributions of other species (Fig. 8, 9, 10, 11) are remarkably more uniform over different longitudes compared with that of water vapor.

Some variations can be seen for ammonia (Fig. 8a and 8b) at 7°N, where enhancements on the east side of brightest regions (including hot spots) are, apparently, recurrent features (Fig. 8c). Here we often observe increases in mixing ratio from about 3.5×10^{-4} to above 5.5×10^{-4}. The overall increase of ammonia toward the equator described in section 4.1 therefore has a longitudinal component. High latitude locations of *water* vapor enhancement found in Fig. 7d are also characterized by moderate increases of ammonia (specifically, from 2×10^{-4} to 3×10^{-4}) in the northern hemisphere (Fig. 8d).

The germane distribution (Fig. 10a and 10b) is non uniform in the North Equatorial Belt around 10°N, since its mixing ratio varies between 5×10^{-10} (60°W) and 8×10^{-10} (310°W). In this latitude, germane is apparently anti-correlated with water vapor and its minima/maxima pattern appears to move between the two Juno's observation periods of PJ1 consistently with wind speeds, as previously noted in this section for water vapor. Noteworthy are also the sharp spatial variations of germane just around the GRS (Fig. 10c and 10d), where the gas mixing ratio appears higher in the central part of the annulus and lower at its internal (toward the GRS itself) and external (toward South Equatorial Belt) boundaries, showing again variations between 5×10^{-10} and 8×10^{-10}. Temporal variations observed in the west side of the annulus between the two planning periods of PJ1 are particularly difficult to justify: while it can be argued that poorer spatial resolution in JM002 allows merging different spatial conditions in the same pixel (averaging therefore extreme values), it seems that JM003 values are consistently higher in areas larger than JM002 pixels. On the other hand, retrieval artefacts also seem unlikely, since other regions observed in both planning periods show similar values in the two maps.

4.3 Relationships between different parameters

The estimates of atmospheric parameters from PJ1 – the perijove with the most complete spatial coverage – allow one to study the mutual relationships among them from a statistical perspective.

For this purpose, we consider the gas abundances (five parameters) retrieved from a given individual spectrum as the coordinates of a point in a five-dimensional space. The overall distribution of points in this space (i.e.: placement of all the spectra in our dataset) fully describes the mutual relationships mentioned above. It is of particular interest to detect, if any, distinct regions of "higher" point density ("clusters"). However, actual implementation of this heuristic concept faces difficulties related to both objective definition of clusters and visual inspection of a space with

any dimension greater than 3. For these reasons, we found the convenient usage of the clustering algorithm described by Campello et al, [2013], as implemented in the HDBSCAN package by McInnes et al., [2015].

HDBSCAN can identify at least seven distinct clusters in the five-dimension space of gas abundances (Fig. 12). Notably, different clusters correspond to distinct latitudinal bands (Fig. 13), confirming, therefore, the prominent importance of large-scale latitudinal variations in driving the composition of the Jupiter's atmosphere, at least at the pressure levels probed by JIRAM data.

Cluster 1 (in purple) corresponds to the central regions of the North Equatorial Belt (8°N-12°N). Spectra in this cluster have a low abundance of phosphine (4.5×10^{-7}) and ammonia (1.25×10^{-4}) and intermediate abundance of germane (6.4×10^{-10}) and intermediate to low abundance of arsine (3×10^{-10}). Water vapor humidity is intermediate to high ($\log_{10}(H_2O)_{RH}$~0.6). The peculiarity of this region has already been noticed in the maps presented by Blain et al. [2018] and Giles et al. [2015].

Cluster 2 (in blue) corresponds to the northern regions of the North Equatorial Belt (12°N-16°N). In comparison to the cluster-1 population, these spectra often display higher water content (probably related to a local meteorology strongly variable in longitude, see Fig. 7c) and, more evident, in phosphine (7.5×10^{-7}). Arsine decreases below 2×10^{-10}. Germane and ammonia content are similar in cluster 1 and cluster 2.

Spectra in cluster 3 (in cyan) are found in the South Temperate Belt (40°S-36.5°S) and to the southern parts of the South Equatorial Belt (south of 17.5°S). Spectra in this cluster have typical contents of phosphine, germane and ammonia very close to the cluster-2 population. The two clusters are however markedly different in their ammonia contents (increased to 2.5×10^{-4} in cluster 3) and, more evident in water vapor ($\log_{10}(H_2O)_{RH}$ decreased to~ -0.4).

Cluster 4 (in green) corresponds to the northern parts of the South Equatorial Belt (12.5°S-9°S). Spectra in this cluster have typical contents of water, phosphine, and arsine very close to the cluster 2 population. Cluster 4 displays however higher typical values for ammonia (increased to 2.5×10^{-4} in cluster 3) and germane (increased to 9×10^{-10}).

Spectra in cluster 5 (in yellow) are found in the southern parts of the South Equatorial Belt (17.5°S-14.5°S), where cluster-3 elements are also frequent. Given the geographical proximity of these two clusters, it is particularly interesting to compare their characteristics. In matter of fact, they are distinguished by the higher water and germane contents observed in cluster 5. While for the latter gas we are still close to the maximum values observed (9×10^{-10}), the content in water vapor in cluster 5 is indeed rather variable and intermediate between the values observed for cluster 2 and 3.

Cluster 6 (in orange) and 7 (in red) elements are typical of polar regions, and in most scatter plots presented in fig. 12 they are clearly distinct from low/intermediate spectra found in other clusters. Polar spectra have higher contents in ammonia, phosphine and arsine and are depleted in germane, consistently to what previously discussed in section 4.1. Cluster 6 and 7 corresponds to South and North poles respectively, albeit some elements of cluster 7 are also found on the southern hemisphere. Again, differences between these two clusters can be anticipated from fig. 5: southern spectra are markedly richer in water, ammonia and arsine.

Noteworthy are also the areas whose spectra do not fall in these main clusters. This implies that the combination of gas content found there is indeed quite uncommon in Jupiter's troposphere. Notable instances are the hot spots, the wake of the Great Red Spot, and the North Temperate Belt. Most of the results of the South Pole observations are also not included in the cluster-6 population.

It should also be noted that most clusters persist even when germane and arsine are removed from the set of parameters used by the classification algorithm. In this case, only the tiny clusters 6 and 5 are removed from the set of detected clusters, being merged with clusters 4 and 7 respectively.

The residual opacity of the 1-bar level is another parameter to be investigated in its relationships with the abundances of minor gases. However, our results derive from data pre-filtered against low-signal cases and refer therefore to conditions of moderate-to-low opacity. Therefore, it is perhaps not surprising that the scatter plots of gas vs. opacity (not shown) do not display any notable trends (albeit global scatter plots are probably not suitable to highlight possible subtle opacity/gas relations in smaller specific areas). Moreover, we observe that the inclusion of opacity among classification parameters does not allow one to distinguish further clusters beyond those described above solely on the basis of gas content.

5. Discussion

5.1 Comparison with previous results

The latitudinal distribution of minor gases at a few bars has been previously described by several authors. Notably, all previous studies discussing conditions at high latitudes had to rely on observations of these regions acquired at high emission angles. JIRAM is the first instrument operating from an highly inclined orbit and therefore capable to observe polar and low latitude areas with comparable viewing geometries.

Giles et al. [2015] presented the large-scale distribution of water vapor between 50°S and 50°N, as derived from data acquired by the VIMS spectrometer – operating in the same spectral range of JIRAM - during the Jupiter Cassini flyby. The most striking difference in comparing against our Fig. 5a is the amplitude of latitudinal maxima, which is found to be 3-5 times larger in JIRAM data. Both Giles et al. and our own retrieval codes include the treatment of multiple scattering, assuming similar values for single scattering albedo and asymmetry factor, therefore aerosol modeling is not a likely source of discrepancy, at least as long as observations are acquired at comparable (small) emission angles. In considering this disagreement one should keep in mind "the relatively low [spatial] resolution [of] VIMS observations. Any small regions of elevated water may be rendered invisible by averaging over the large areas covered by the VIMS pixels" (Giles et al. [2015]). Such limited regions are indeed found in Fig. 7c and 7d, while high spatial resolution map presented by Roos-Serote et al., [2000] from NIMS Galileo data quantitatively confirms the occurrence of very humid regions (relative humidity >> 20%) west and north of hot spots, as seen at the center of our Fig. 7c. In the comparison between VIMS- and JIRAM-derived profiles, we note also the fair correspondence in the positions of latitudinal maxima (especially for the VIMS night-side data) for latitudes covered by the two datasets. In both cases, the main peak is found in the South Equatorial

Belt (between 10°S and 5°S), at the rim of Equatorial Zone; further maxima in the North Equatorial Belt (between about 7°N and 15°N) as well as at 26°N and 35°N are other shared features. On the other hand, VIMS data do not show the smaller (and more variable) peaks seen by JIRAM at 43°S, 35°S, possibly 'diluted' by the large VIMS pixel size. The VIMS peak at 25°S occurs over a region of thick cloud coverage and is not covered by our pre-filtered JIRAM retrievals. Local increases of water vapor in cyclonic regions are consistent with the models presented in Dowling and Gierasch [1989] and Fletcher et al., [2017], where pressures cause the lifting of condensation level and the water cloud to bulge upwards, promoting moist convection.

The increase of ammonia at both borders of the Equatorial Zone and the strong depletion observed at 10°N are in qualitative and quantitative agreement with the measurements of the Juno Microwave Radiometer (MWR) described by Li et al., [2017], as already noted on a much more limited subset of JIRAM retrievals presented by Orton et al. [2017]. An ammonia enhancement over the Equatorial Zone was previously described on the basis of data from Voyager IRIS [Gierasch et al., 1986], Cassini CIRS and IRTF/TEXES [Achterberg et al., 2006; Fletcher et al., 2016], but all these estimates refer to pressure well below the 1-bar level, therefore to an altitude much higher than the one probed by JIRAM. Blain et al., [2017] presented ammonia estimates at the approximate level of 2 bar (about 0.8 scale height above the region of the JIRAM peak sensitivity at 4.5 bar) on the basis of ground-based, high-spectral resolution (resolving power about 13,000) IRTF-TEXES measurements in the 5.146-5.181 μm spectral range. Their figure 11 indicates a larger latitudinal width of the 10°N depletion once compared against our Fig. 8b and lack any indication of a strong increase toward the center of Equatorial Zone. On the other hand, their mean values between 40°S and 10°S and 25°N and 40°N are in excellent agreement with our findings (2.5×10^{-4}). This is in contrast with the results presented in Giles et al,. [2017b] from CRIRES-VLT data in the 5.152-5.188 μm spectral range at a spectral resolving power of 96,000. These authors presented a latitudinal profile at 3.3 bar where, in North and South Equatorial belts (around 15°S and 10°N), the ammonia mixing ratio is typically twice what we find, and falls below 1×10^{-4} in the most opaque latitudes (where our coverage is strongly biased toward the few clear areas there). A joint analysis of these datasets (beyond the scope of this paper) is required to reconcile these results. Significant longitudinal variations of ammonia at the hot spot latitudes were previously reported by de Pater et al., [2016, Fig 2d there], for pressures comparable to those sampled by JIRAM data. Ammonia plumes were previously reported by Fletcher et al., [2016] southeast of hotspots at the approximate level of 0.5 bar and are observed also in MWR data [Fletcher et al., 2019]. These plumes however appear very dark at 5μm (thick clouds) and are not expected to be covered directly by our retrievals. Therefore, enhancements seen in Fig. 8c probably represent only the initial part of an eastward increase of ammonia from the depleted hot spot centers that culminates in plumes.

Our results on phosphine are generally consistent with the latitudinal trends presented in Fig. 17 of Giles et al, [2017a] for the dataset they acquired on 1 January 2013 at CRIRES-VLT observing in the 5.065-5.08 μm range. The relatively constant value around 7.5×10^{-10} between 40°S and 20°S (contrary to what observed by the same authors on 12 November 2012), the slow rise to about 1×10^{-9} at 35°N as well as the minimum to 4.5×10^{-10} around 10°S presented by these authors have fair correspondence with our Fig. 5c. Our phosphine increase between 15°S and 5°S is in

quantitative agreement with 12 November 2012 CRIRES-VLT data, but not with later observations by the same instrument. An increase toward the equator was previously reported from Cassini CIRS and IRTF/TEXES data [Fletcher et al., 2009, Fletcher et al., 2016]. The latter paper also shows a phosphine content at intermediate latitudes (30°-60°) higher on the northern hemisphere than on the southern one, as also seen in our Fig. 5c, but again both studies refer to higher levels in the atmosphere than the ones probed by our retrievals. JIRAM data are also consistent with phosphine latitudinal profiles derived from Cassini VIMS maps presented in Giles et al., [2015] (Fig. 14b there), notably considering the region between 40°N and 50°N where both datasets suggest values slightly lower than 1×10^{-9}. Quantitative correspondence exists also for the 10°N minimum, while three other minima found in VIMS data at 0°, 30°N, and 25°N fall on cloud-thick zones not covered by our retrievals. The VIMS-derived maximum of 1×10^{-9} at 40°S is not confirmed neither by our retrievals nor by Giles et al, [2017a]. Drossart et al., [1990] previously described latitudinal trends of phosphine from ground-based data in the same 5.07 μm range used by Giles et al, [2017a]. Despite the coarse spatial resolution of these historical observations, we note that the enhancement measured in the "Northern region" "between about 40°N and 60°N" are consistent - within error bars - with our own estimates, while the value reported for the North Equatorial Belt is definitively higher than the depletion we observe at 10°N.

A significant disagreement exists between our retrievals and strong phosphine increases poleward of 60°N and 50°S described in Giles et al., [2017a]. In the northern hemisphere this discrepancy is even more relevant, since the high mean radiance poleward of 60°N implies a lesser degree of bias in our results due to our filter against low-radiance (i.e.: cloudy) cases. Comparison of retrievals from CRIRES-VLT data with different assumption on deep cloud presented by Giles et al, [2017a] demonstrates that poleward increases are not a result of these assumptions. Similarly, our attempt to introduce a deep cloud did not induce any remarkable phosphine increase toward the poles. Differences in vertical sensitivity are also unlikely: although Giles et al, [2017a] did not present a specific discussion on the shape of weighting functions in CRIRES-VLT data for the phosphine feature considered in their study, Fig. 2f in Grassi et al, [2010] suggests that the feature at 5.07 μm is a relatively weak one, probing altitudes higher than the peak of JIRAM sensitivity for phosphine (see Grassi et al, [2010], fig. 3c). The two datasets together would suggest in this case an *increase* with altitude of phosphine at high latitudes, contrary to what is reasonably expected for a disequilibrium species mixed from below, unless a possible photochemical source might add to the PH_3 abundance at the higher altitudes. Finally, we remind again the high emission angles ($\varepsilon>60°$) at which regions poleward of 60°N were observed in data used by Giles et al, [2017a], that increases the path length through the aerosols with respect to the JIRAM observations.

Giles et al, [2017a] described also the latitudinal trends of germane from its features in the 4.6-4.7 μm range in CRIRES-VLT data. Once compared against our Fig. 5d, a very good agreement is found in the positions and relative amplitudes of maxima at 40°S, 15°S, 15°N and 30°N. Although our retrievals do not extend over cloud-thick zones, the marked decreases observed at their boundaries are in agreement with deep minima found by Giles et al, [2017a]. It would be tempting to explain quantitative systematic differences in JIRAM and CRIRES-VLT germane values at these latitudes on the basis of different correction factors applied to STDS line intensities by the two

teams, since Giles et al. [2017a] considered as reference the GEISA values instead of Schaeffer & Lovejoy [1985]. However, in our own attempt to use GEISA data, this seems to amplify the differences rather than reducing them. An interesting discrepancy is observed, once again, at high latitudes, poleward of 40°N and 40°S, namely that the maxima found by Giles et al., [2017b] are completely missing in JIRAM retrievals. Similar considerations as presented above for phosphine may apply, but JIRAM and CRIRES-VLT both rely on the same spectral feature (albeit at very different spectral resolution) and therefore differences in the vertical position of peak sensitivity are rather unlikely for the germane analysis. It shall be mentioned that Giles et al., [2017b] found that an equally good spectral fit of their data can be achieved keeping the gemane mixing ratio fixed to the value observed in the South Equatorial Belt and allowing the optical depth of a deep 5-bar cloud to vary. As previously mentioned in section 3, a similar test on JIRAM data resulted in an opposite outcome, with a statistically significant deterioration of the fit. JIRAM data support therefore the view that germane latitudinal trends are indeed real features and not a result of degeneracy.

The Giles et al, [2017a] analysis shows the same JIRAM latitudinal trends of arsine (Fig. 5e). In this case, the poleward increase found from CRIRES-VLT data is confirmed quantitatively by JIRAM retrievals. Also the peaks at 50°S and 10°N (and possibly 20°N) are found in both datasets, albeit with different absolute values. Once again, our lack of estimates in cloud-thick zones does not allow us to confirm the very low values of disequilibrium gases found by Giles et al, [2017a] there.

5.2 Relative abundances of disequilibrium species: implications for vertical mixing

The classic interpretation of the elevated abundances of PH_3, GeH_4, and AsH_3 is that they reflect vertical mixing upward from a region deeper in Jupiter's atmosphere where the temperatures are high enough that chemical equilibration is achieved [e.g. Fegley and Prinn, 1985]. The abundance of a given disequilibrium species is set by the requirement that chemical equilibration ceases at a depth above which the timescale for chemical equilibration is equal to the vertical mixing timescale. Because the chemical equilibration timescale is governed by rate equations that typically depend exponentially on inverse temperature, while the vertical mixing timescale is only weakly dependent on temperature, equating the two timescales leads to a sharp boundary above which the reactions are "quenched" and the abundance of the species—expressed as mixing ratio relative to molecular hydrogen—is fixed [e.g. Visscher and Moses, 2011]. The typical temperature range for quenching of these species measurable in Jupiter's atmosphere are in the 500-1000 K range, so their observed abundances probe the chemical conditions down to pressures approaching a kilobar.

Complications in using disequilibrium species in this manner include the presence of photochemically altered abundances, uncertainty in the strength of vertical mixing, and lack of experimental knowledge of rates of key chemical reactions. The first of these is ameliorated through observing as deeply as possible in the observable troposphere, hence at wavelengths near 5 μm, as JIRAM does. The second can be resolved by looking simultaneously at multiple disequilibrium species, fitting their abundances for the strength of vertical mixing expressed as a single coefficient, the vertical eddy mixing coefficient K which has units of length-squared/time. Thus, in this scheme all vertical mixing processes are parametrized as a single diffusive process, but with an efficiency far exceeding that for molecular diffusion. Typical eddy mixing values that provide a reasonable fit

to CO, for example, in Jupiter's troposphere are in the 10^6-10^9 cm^2/s range and likely varies with latitude. The uncertainty in reaction rates is more problematic for some disequilibrium species than others; data for PH_3 are better known than for GeH_4 and AsH_3, but the germane kinetics data are somewhat better than for arsine [Wang et al., 2016].

The results described in this paper for the abundance and latitudinal distribution of PH_3, GeH_4, and AsH_3 can therefore be used in a preliminary way to probe the conditions in the kilobar regions of Jupiter's atmosphere. Wang et al. [2016] modeled the latitudinal abundances of these species using a one-dimensional diffusion-kinetics model, but allowing the vertical mixing coefficient K to vary with latitude according to a scheme formulated in Wang et al. [2016] based on turbulent rotating convection.

Figure 16 of Wang et al., shows a predicted abundance with latitude of quenched GeH_4 in the observable troposphere. It is constant from the equator to ±30°, followed by a decline in abundance by a factor of 2 up to 80°, where it levels out. This is consistent, within the error bars, with the observed behavior of germane in the JIRAM data shown in figure 5d. Fitting the low-latitude mixing ratio in the JIRAM data of $\sim 7\times10^{-10}$ requires an equatorial eddy mixing coefficient of $K \sim 10^8$ cm^2/s (figure 12 of Wang et al,, [2016]), suggestive of high but reasonable vertical mixing rates. Conversely, the PH_3 abundance dependence on K becomes very weak for $K > 10^7$ cm^2/s, and is predicted by Wang et al to have a mixing ratio of 7×10^{-7}, independent of latitude (their figure 7). This is quite close to the value derived by JIRAM of 8×10^{-7}, and indeed the observed mixing ratio shows only a weak dependence on latitude at best. Thus, the phosphine and germane abundances derived by JIRAM fit well the model of disequilibrium species transported upward from the deep troposphere by vigorous vertical mixing.

On the other hand, the AsH_3 data, while well fitted at low latitudes by the 2×10^{-10} mixing ratio predicted by the Wang et al. [2016] model, show a strong increase at high latitudes to a value over 3 times higher. As already observed by Giles et al., [2017b], this is not predicted by Wang et al., because the arsine abundance is constant with eddy mixing coefficients for essentially all values of the latter (their figure 14). Wang et al. noted that the kinetics of arsine conversion are the most poorly known of the three disequilibrium species considered here, and so it is possible that the sensitivity of arsine to the value of K is in fact much stronger than predicted by Wang et al. [2016]. The direction of that effect would have to be such that, as K weakens toward the poles, AsH_3 increases in abundance. Alternatively, the vertical mixing could be much stronger as one approaches the poles, but this is contradicted by the good fit of the germane mixing ratio curve to the JIRAM data with latitude using a value of K from Wang et al. [2015] that declines toward the poles. The close correspondence of the JIRAM value from equatorial to mid-latitudes with that predicted by Wang et al. [2015] model suggests that the kinetics are reasonably correct. Hence the strong upturn of arsine at polar latitudes seen by JIRAM cannot be explained by the diffusion-kinetics model. This is most likely related to the 1D assumption, that cannot capture the complexity of horizontal motions that may play a role in the final distribution of gaseous species.

Conclusions

The analysis of JIRAM 5-μm data presented in this paper supports the view of significant horizontal variations in the mixing ratios of minor gases in the troposphere of Jupiter at the level of few bars.

At the current date, most of the observed trends remain unexplained, and indeed our work aimed mostly to provide further experimental reference for more advanced theoretical elaboration, that remains however beyond the purpose of this effort.

Previous results by several other authors [notably Giles et al., 2015, 2017a, 2017b, Li et al., 2017] at comparable pressure levels are placed in a more general context, providing simultaneous retrievals for water vapor, ammonia, phosphine, germane and arsine at relatively high spatial resolution (better than 500 km) and low emission angles (<40°).

Horizontal variations of gases are dominated by latitudinal components, whose patterns are remarkably constant over the two years period covered by our data. Automatic classification of retrievals returns clusters located at distinct latitudes. Longitudinal variations are relatively more important for water vapor and, in lesser extent, for ammonia and germane. At the northern rim of the North Equatorial Belt and in polar regions, local enhancements of water vapor are apparently associated with infrared-bright cyclonic structures, in agreement with the scheme proposed by Dowling and Gierasch [1989]. Mean latitudinal profiles of water vapor relative humidity at intermediate latitudes display also intriguing relations with global wind patterns inferred from visible images by Porco et al.,[2003], suggesting again enhancement in cyclonic belts.

Our retrievals are biased toward relatively cloud-free regions, and consequently the present analysis does not allow us to infer unambiguous relationships between cloud opacities and the content of condensable gases (water and ammonia). A comparison of the JIRAM-derived latitudinal profiles of disequilibrium species (phosphine, germane and arsine) against the expectations of the model by Wang et al. [2016] identifies a disagreement for arsine, confirming the same remark by Giles et al. [2017a], and pointing toward the need of more complex spatial modeling of eddy diffusion in future theoretical efforts.

The main limit of our analysis is the accuracy of the forward model used to simulate spectra. Its performances are comparable to similar tools largely employed in literature [e.g. Irwin et al., 2007] but still not adequate to model JIRAM data within their extremely low nominal noise equivalent radiance.

The present work does not provide any clear evidence of the occurrence of a deep cloud at the level of about 5 bars [Bjoraker et al., 2015]. While specific test runs demonstrated that retrieved latitudinal profiles of gas mixing ratios do not substantially depend on the inclusion of such a structure in the model, its occurrence can be investigated in future efforts when more sophisticated forward models will be adopted.

Acknowledgements

This work was supported by the Italian Space Agency through ASI-INAF contract 2016-23-H.1-2018.

S. Atreya and J. Lunine were supported through the Juno Project.

L. Fletcher was supported by a Royal Society Research Fellowship and European Research Council Consolidator Grant (under the European Union's Horizon 2020 research and innovation programme, grant number 723890) at the University of Leicester.

G. Orton was supported by NASA funding to the Jet Propulsion Laboratory, California Institute of Technology.

JIRAM has been developed by Leonardo S.p.A. at the Officine Galileo - Campi Bisenzio site.

We thank N. Ignatiev (IKI, Moscow) for the permission to use his radiative transfer subroutines and his kind help in code development.

We thank M. D'Amore (DLR, Berlin) and E. D'Aversa (IAPS-INAF, Rome) for their suggestions on data clustering.

JIRAM data used for this analysis are available at the NASA Planetary Data System as dataset *JNO-J-JIRAM-3-RDR-V1.0* [Noschese and Adriani, 2017]

https://pds-atmospheres.nmsu.edu/data_and_services/atmospheres_data/JUNO/jiram.html

Retrieval results presented in this analysis are available at http://dx.doi.org/10.17632/cjs32jv68g.1

JIRAM was conceived and brought to reality by our late collaborator and institute director Dr. Angioletta Coradini (1946-2011).

References

Achterberg, R. K., et al., (2006) *Cassini CIRS retrievals of ammonia in Jupiter's upper troposphere*, Icarus, 182, doi: 10.1016/j.icarus.2005.12.020

Adriani, A., et al. (2014) *JIRAM, the Jovian Infrared Auroral Mapper,* Space Sci. Rev., doi:10.1007/s11214-014-0094-y

Adriani, A., et al. (2016) *Juno's Earth flyby: the Jovian infrared Auroral Mapper preliminary results*. Astrophysics and Space Science, 361, doi: 10.1007/s10509-016-2842-9

Adriani, A., et al. (2019) *Two-years observations of the Jupiter polar regions by JIRAM on board Juno*, submitted to J. Geophys. Res.

Antuñano, A., et al. (2018) *Infrared characterization of Jupiter's equatorial disturbance cycle*, Geophysical Research Letters, 45, doi: 10.1029/2018GL080382

Archinal, B. A., et al. (2011) *Report of the IAU Working Group on Cartographic Coordinates and Rotational Elements: 2009* Celestial Mechanics and Dynamical Astronomy, 109, 101-135 doi:10.1007/s10569-010-9320-4

Atreya, S. K., et al. (1999) *A comparison of the atmospheres of Jupiter and Saturn: deep atmospheric composition, cloud structure, vertical mixing, and origin*, Planetary and Space Science, 47 (10–11), doi:10.1016/S0032-0633(99)00047-1

Bjoraker, G. L., et al. (2015) *Jupiter's deep cloud structure revealed using Keck observations of spectrally resolved line shape*, The Astrophysical Journal, 810 (2), doi: 10.1088/0004-637x/810/2/122

Blain, D., et al. (2018) *Mapping of Jupiter's tropospheric NH_3 abundance using ground-based IRTF/TEXES observations at 5 μm*, Icarus, 314, doi: 10.1016/j.icarus.2018.06.002

Bolton, S., et al. (2017) *Jupiter's interior and deep atmosphere: The initial pole-to-pole passes with the Juno spacecraft,* Science, 356 (6340), doi: 10.1126/science.aal2108

Boudon, V., et al. (2018) *Line positions and intensities for the v_3 band of 5 isotopologues of germane for planetary applications*, Journal of Quantitative Spectroscopy and Radiative Transfer, 205, doi: 10.1016/j.jqsrt.2017.10.017

Campello, R., et al., (2013) *Density-Based Clustering Based on Hierarchical Density Estimates*, In *Pacific-Asia Conference on Knowledge Discovery and Data Mining*, 160–72, Springer. Doi: 10.1007/978-3-642-37456-2_14

Conrath, B. J., et al. (1998) *Thermal Structure and Para Hydrogen Fraction on the Outer Planets from Voyager IRIS Measurements*, Icarus, 135 (2), doi: 10.1006/icar.1998.6000

de Pater, I., et al. (2016) *Peering through Jupiter's clouds with radio spectral imaging*, Science, 352 (6290), doi: 10.1126/science.aaf2210

Dowling, T.E. and P.J. Gierasch, P.J. (1989) *Cyclones and Moist Convection on Jovian Planets*, Bulletin of the American Astronomical Society, 21

Drossart, P., et al. (1990) *Jupiter: Evidence for a Phosphine Enhancement at high Northern latitudes*, Icarus, 83, doi:10.1016/0019-1035(90)90018-5

Drossart, P., et al. (1998) *The solar reflected component in Jupiter's 5-μm spectra from NIMS/Galileo observations*, J. Geophys. Res., 103 (E10), doi:10.1029/98JE01899

Fegley, B., and Prinn, R. G. (1985) *Equilibrium and nonequilibrium chemistry of Sat- urn's atmosphere—Implications for the observability of PH_3, N_2, CO, and GeH_4*, The Astrophysical Journal, 299, doi: 10.1086/163775

Fegley, B., and Prinn, R. G. (1988) *Chemical constraints on the water and total oxygen abundances in the deep atmosphere of Jupiter,* The Astrophysical Journal, 324, doi: 10.1086/165922

Fletcher, L. N. et al. (2009) *Phosphine on Jupiter and Saturn from Cassini/CIRS*, Icarus, 202 (2), doi: 10.1016/j.icarus.2009.03.023

Fletcher, L. N., et al. (2016) *Mid-infrared mapping of Jupiter's temperatures, aerosol opacity and chemical distributions with IRTF/TEXES*, Icarus, 278, doi:10.1016/j.icarus.2016.06.008

Fletcher, L. N. (2017a) *Cycles of activity in the Jovian atmosphere*, Geophys. Res. Lett., 44, doi:10.1002/2017GL073806.

Fletcher, L. N. et al., (2017) *Moist convection and the 2010–2011 revival of Jupiter's South Equatorial Belt*, Icarus, 286, doi: 10.1016/j.icarus.2017.01.001.

Fletcher, L. N. et al., (2019) *Jupiter's Ammonia-Rich Equatorial Plumes*, contribution 453-1 to the EPSC-DPS Joint Meeting 2019, https://meetingorganizer.copernicus.org/EPSC-DPS2019/EPSC-DPS2019-453-1.pdf

Gierasch, P. J., et al. (1986) *Zonal mean properties of Jupiter's upper troposphere from Voyager infrared observations*, Icarus, 67, doi: 10.1016/0019-1035(86)90125-9

Giles, R. S., et al. (2015) *Cloud structure and composition of Jupiter's troposphere from 5-μm Cassini VIMS spectroscopy*, Icarus, 257, doi:10.1016/j.icarus.2015.05.030

Giles, R. S., et al. (2017a) *Latitudinal variability in Jupiter's tropospheric disequilibrium species: GeH_4 , AsH_3 and PH_3*, Icarus, 289, doi:10.1016/j.icarus.2016.10.023

Giles, R. S., et al. (2017b) *Ammonia in Jupiter's troposphere from high - resolution 5 μm spectroscopy*, Geophys. Res. Lett., 44, doi:10.1002/2017GL075221

Gordon, I. E., et al. (2017) *The HITRAN2016 molecular spectroscopic database*, Journal of Quantitative Spectroscopy and Radiative Transfer, 203, doi: 10.1016/j.jqsrt.2017.06.038

Grassi, D., et al. (2010) *Jupiter's hot spots: Quantitative assessment of the retrieval capabilities of future IR spectro-imagers*, Planetary and Space Science, 58, doi:10.1016/j.pss.2010.05.003.

Grassi, D., et al. (2017a) *Preliminary results on the composition of Jupiter's troposphere in hot spot regions from the JIRAM/Juno instrument,* Geophys. Res. Lett., 44, doi: 10.1002/2017GL072841

Grassi, D., et al. (2017b) *Analysis of IR-bright regions of Jupiter in JIRAM-Juno data: Methods and validation of algorithms,* Journal of Quantitative Spectroscopy and Radiative Transfer, 202, doi: 10.1016/j.jqsrt.2017.08.008

Ingersoll, A. P., et al. (2004) *Dynamic of Jupiter's atmosphere*, in *Jupiter, the Planet, Satellite and Magnetosphere,* Bagenal, Dowling and McKinnon ed., Cambridge University Press, ISBN 0521818087

Irwin, P. G. J., et al. (1998), *Cloud structure and atmospheric composition of Jupiter retrieved from Galileo near-infrared mapping spectrometer real-time spectra,* J. Geophys. Res., 103(E10), doi:10.1029/98JE00948

Irwin, P. G. J., et al. (2001), *The Origin of Belt/Zone Contrasts in the Atmosphere of Jupiter and Their Correlation with 5-μm Opacity*, Icarus, 149, doi:10.1006/icar.2000.6542

Irwin, P. G. J., et al. (2007), *The NEMESIS planetary atmosphere radiative transfer and retrieval tool,* Journal of Quantitative Spectroscopy and Radiative Transfer, 109, 1136-1150, doi: 10.1016/j.jqsrt.2007.11.006

Jacquinet-Husson, N., et al. (1999) *The 1997 spectroscopic GEISA databank*, Journal of Quantitative Spectroscopy and Radiative Transfer, 62, doi: 10.1016/S0022-4073(98)00111-3

Kylling, A., et al. (1995) *A reliable and efficient two-stream algorithm for spherical radiative transfer: Documentation of accuracy in realistic layered media*, J. Atmos. Chem., 21, 115-150, doi:10.1007/BF00696577

Li, C., et al. (2017) *The distribution of ammonia on Jupiter from a preliminary inversion of Juno microwave radiometer data*, Geophys. Res. Lett., 44, doi:10.1002/2017GL073159

McInnes, L., et al., (2017) *Hdbscan: Hierarchical density based clustering*, Journal of Open Source Software, 2(11), 205, doi: 10.21105/joss.00205

Noschese, R., and Adriani, A., (2017), *JNO-J-JIRAM-3-RDR-V1.0*, NASA Planetary Data System, https://pds-atmospheres.nmsu.edu/data_and_services/atmospheres_data/JUNO/jiram.html

Orton, G. S., et al. (2017). *Multiple-wavelength sensing of Jupiter during the Juno mission's first perijove passage*. Geophys. Res. Lett., 44, doi: 10.1002/2017GL073019

Porco, C., et al., (2003), *Cassini imaging of Jupiter's atmosphere, satellites, and rings*. Science, 299 (5612), 1541-1547, doi: 10.1126/science.1079462

Prinn, R. G., and Barshay, S. S. (1977) *Carbon monoxide on Jupiter and implications for atmospheric convection,* Science, 198 (4321), doi: 10.1126/science.198.4321.1031-a

Robinson, T. D., and Catling, D. C., (2013) *Common 0.1 bar tropopause in thick atmospheres set by pressure-dependent infrared transparency,* Nature Geoscience, 7, doi: 10.1038/ngeo2020

Rodgers, C. R. (2000) *Inverse Methods for Atmospheric Sounding: Theory and Practice*, World Scientific, Singapore, ISBN: 9789810227401

Rogers, J. H., (2009) *The Giant Planet Jupiter*, Cambridge University Press, ISBN-13: 978-0521115308

Roos-Serote, M., et al. (1998) *Analysis of Jupiter north equatorial belt hot spots in the 4–5 μm range from Galileo/near-infrared mapping spectrometer observations: Measurements of cloud opacity, water, and ammonia*, J. Geophys. Res., 103(E10), doi:10.1029/98JE01049

Roos-Serote, M., et al. (2000) *Proximate humid and dry regions in Jupiter's atmosphere indicate complex local meteorology*, Nature, 405, doi: 10.1038/35012023

Schaeffer, R. D. & Lovejoy, R.W. (1985) *Absolute line strengths of $^{74}GeH_4$ near 5 μm*, Journal of Molecular Spectroscopy, 113, doi: 10.1016/0022-2852(85)90270-X.

Seiff, A. et al. (1998) *Thermal structure of Jupiter's atmosphere near the edge of a 5-μm hot spot in the north equatorial belt*, J. Geophys. Res., 103 (E10), doi: 10.1029/98JE01766. Available as numerical data as GP-J-ASI-3-ENTRY-V1.0, NASA Planetary Data System

Showman, A. P., and Ingersoll, A. P.(1998)*Interpretation of Galileo Probe Data and Implications for Jupiter's Dry Downdrafts*, Icarus, 132, doi:10.1006/icar.1998.5898.

Siegel, S. (1956) *Non-parametric statistics for the behavioral sciences,* McGraw-Hill, ISBN: 0070856893

Sindoni, G., et al. (2017) *Characterization of the white ovals on Jupiter's southern hemisphere using the first data by the Juno/JIRAM instrument*. Geophys. Res. Lett., 44, doi: 10.1002/2017GL072940

Stamnes, K., et al. (1998) *Numerically stable algorithm for discrete-ordinate-method radiative transfer in multiple scattering and emitting layered media*, Appl. Opt., 27 (12), 2502–2509, doi: 10.1364/AO.27.002502

Taylor, F. W., et al. (2004) *The Composition of the Atmosphere of Jupiter*, in *Jupiter, the Planet, Satellite and Magnetosphere,* Bagenal, Dowling and McKinnon ed., Cambridge University Press, ISBN 0521818087

Tollefson, J., M. H., et al. (2017) *Changes in Jupiter's zonal wind profiles preceding and during the Juno mission,* Icarus, 296, doi: 10.1016/j.icarus.2017.06.007.

Visscher, C., and Fegley, B. (2005) *Chemical constraints on the water and total oxygen abundances in the deep atmosphere of Saturn,* The Astrophysical Journal, 623, doi: 10.1086/428493

Visscher, C., and Moses, J. I. (2011) *Quenching of carbon monoxide and methane in the atmospheres of cool brown dwarfs and hot Jupiters,* The Astrophysical Journal, 783 (1), doi: 10.1088/0004-637X/738/1/72

Wallace, J., and Hobbs, P. (2006) *Atmospheric Science. An Introductory Survey*, Elsevier, ISBN: 9780127329512

Wang, D., et al. (2015) *New insights on Jupiter's deep water abundance from disequilibrium species,* Icarus, 250, doi: 10.1016/j.icarus.2014.11.026

Wang, D., et al. (2016) *Modeling the disequilibrium species for Jupiter and Saturn: Implications for Juno and Saturn entry probe,* Icarus, 276, doi: 10.1016/j.icarus.2016.04.027

Wenger, Ch., and Champion, J. P. (1998) *Spherical top data system (STDS) software for the simulation of spherical top spectra*, Journal of Quantitative Spectroscopy and Radiative Transfer, 59, doi: 10.1016/S0022-4073(97)00106-4

Young, R. M. B., et al. (2018) *Simulating Jupiter's weather layer. Part I: Jet spin-up in a dry atmosphere,* Icarus, 326, doi: 10.1016/j.icarus.2018.12.005

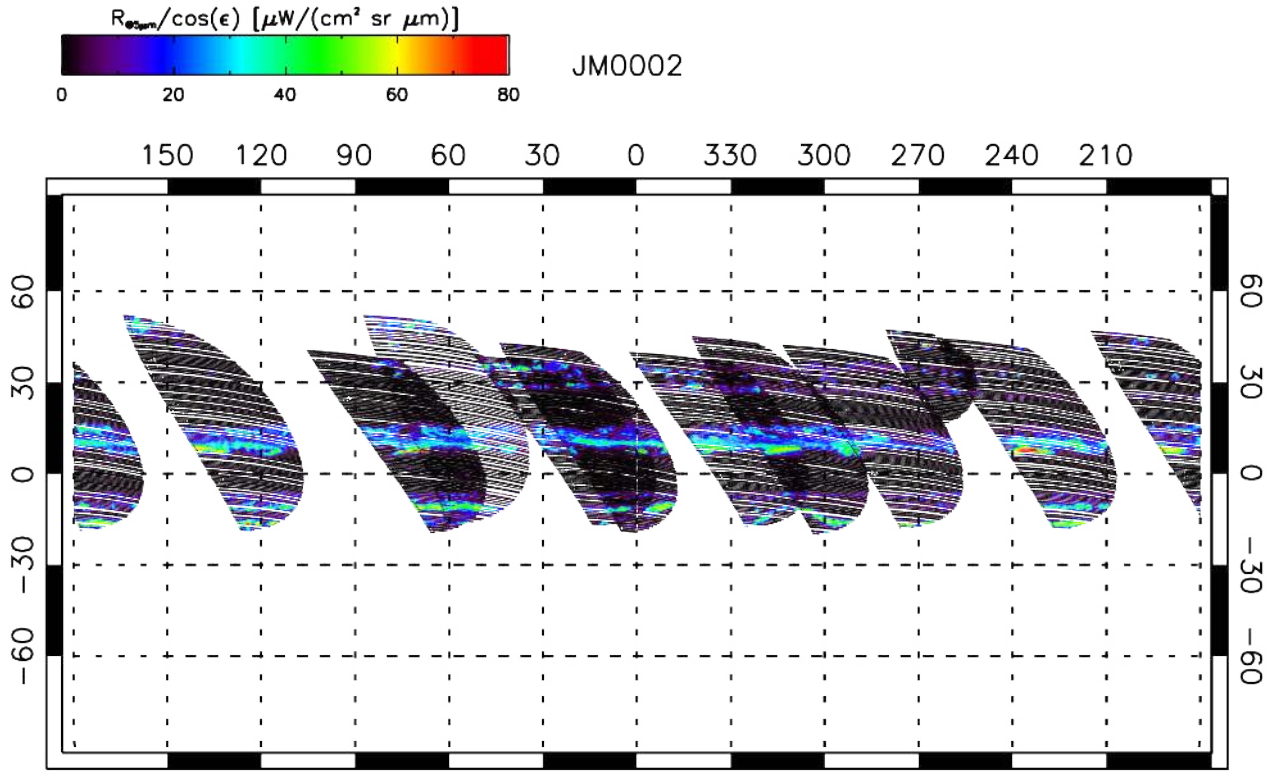

Fig. 1a

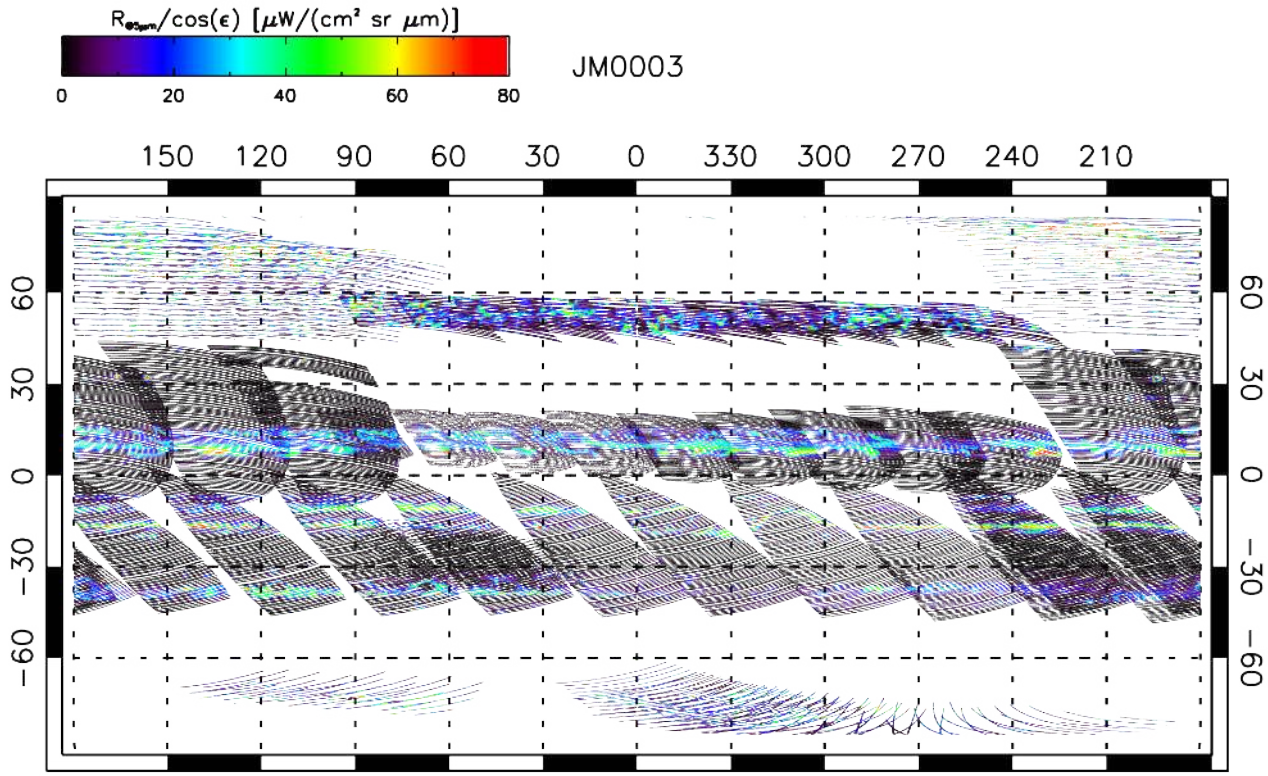

Fig. 1b

Figure 1. Spatial coverage of JIRAM spectrometer measurements around the first Juno perijove passage(PJ1, Aug. 27th, 2016, 12:50 UTC).
Fig. 1a. Planning period JM0002 - approaching segment of the orbit - until Aug. 26th, 10:58 UTC.
Fig. 1b. Planning period JM0003 - maximum approach segment - after Aug. 26th, 10:58 UTC.
The two panels present only cases with emission angles less than 40° and a field of view smaller than 500 km. Color code gives the signal measured at 5 μm (divided by the cosine of emission angle ε). Only spectra with a signal above 20 μW/(cm^2 sr μm) were retained for the retrieval of minor gases. Coordinate system III with planetocentric latitudes is adopted.

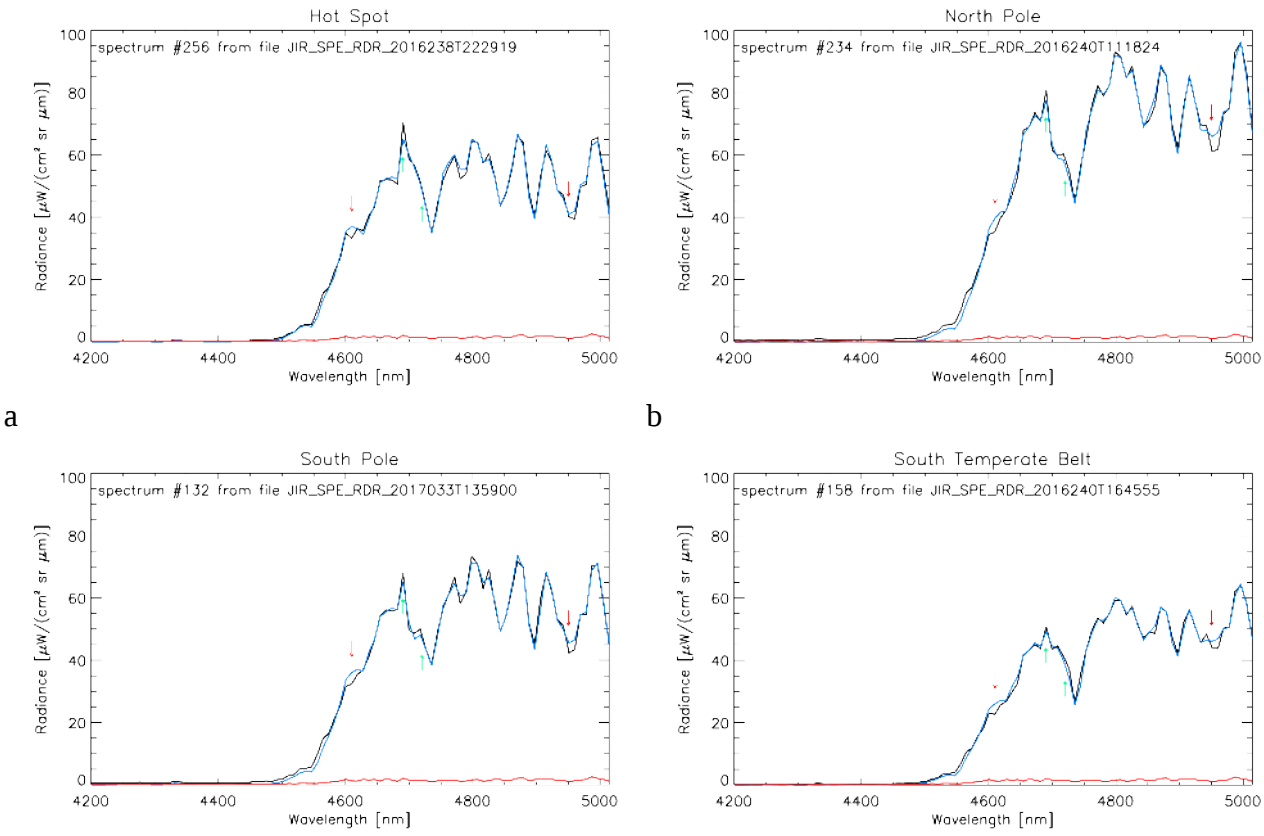

Figure 2. Examples of spectra fits produced by the retrieval code. Black: JIRAM data, blue: best fit spectrum, red: effective noise level, inclusive of forward model errors. The label in each panel identifies the JIRAM spectrum in the dataset stored at the NASA Planetary Data System [Noschese & Adriani, 2017]. The arrows show the locations of common occurrence of misfits described in the text.

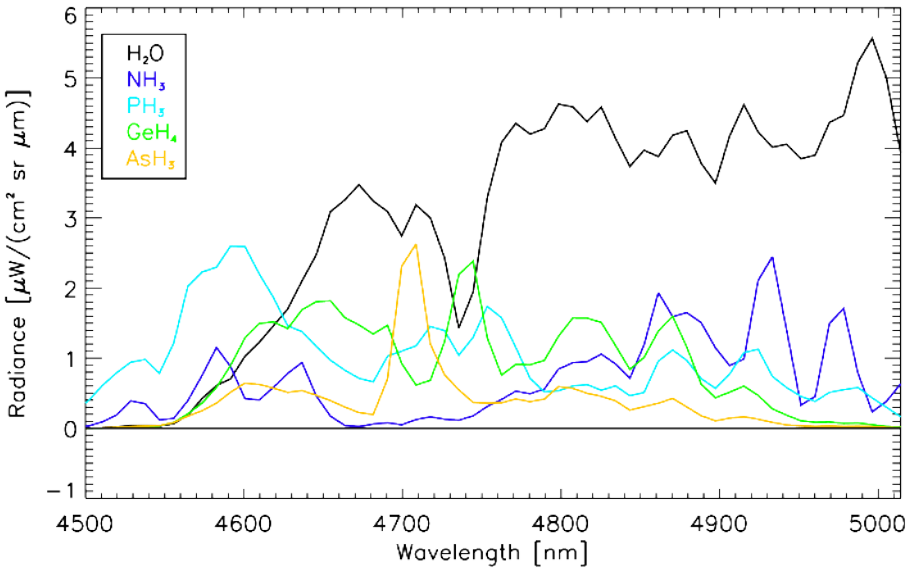

Figure 3. Expected effects on a bright spectrum (τ=0.1, e.g.: fig. 2b) of gas variations corresponding to the 1-σ retrieval uncertainties quoted in the text. The different curves present the signal increase (not the absolute signal) obtained by decreasing (separately) the content of each gas of an amount corresponding to its 1-σ retrieval uncertainty. The horizontal black curve provides the zero level.

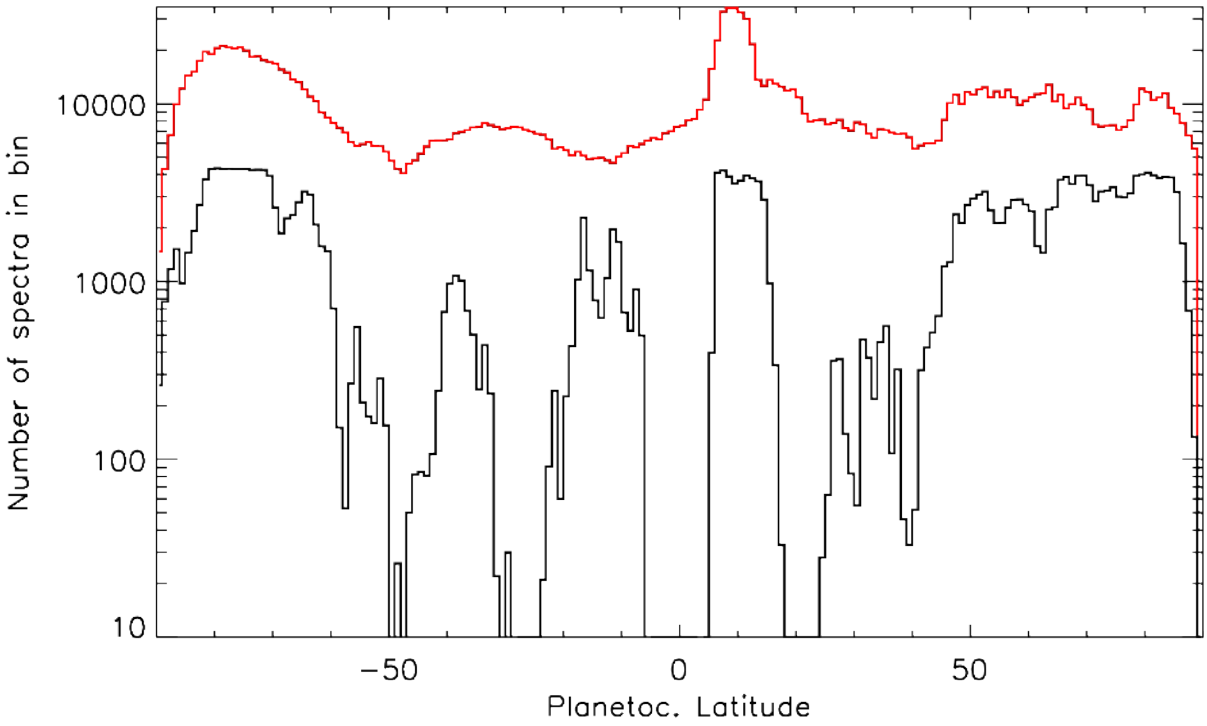

Fig. 4a

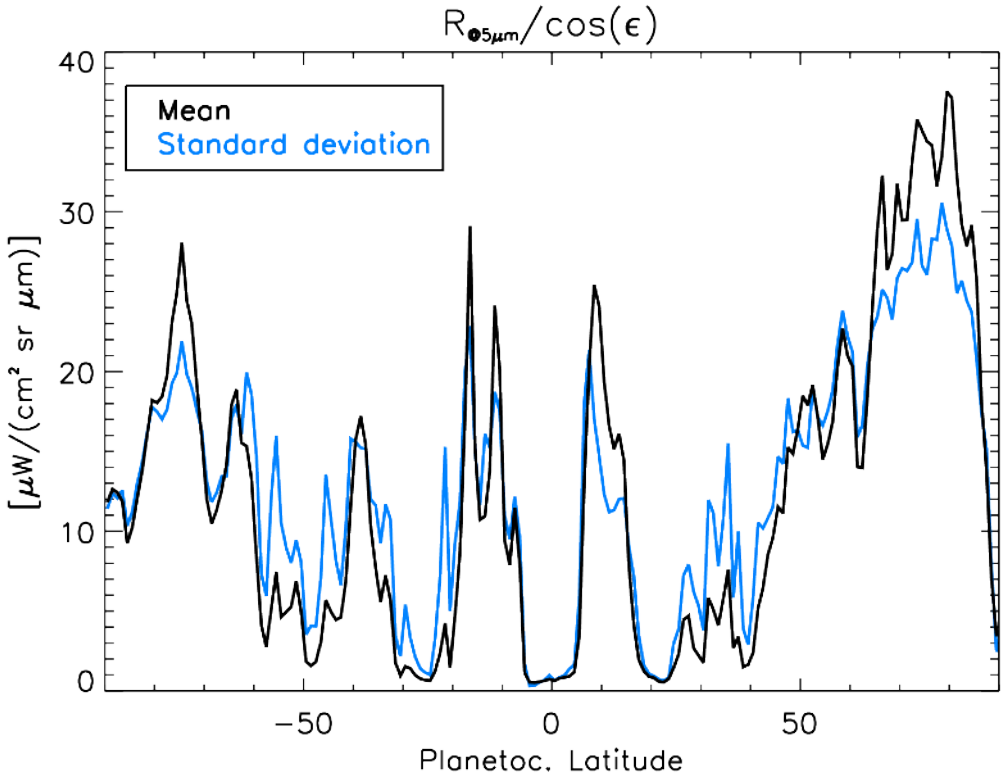

Fig. 4b

Figure 4. Data size and distribution.
Fig. 4a. Black curve: latitudinal distribution for the spectra considered in this study (bin size = 1°); red curve: latitudinal distribution of the spectra in the entire JIRAM dataset (i.e.: prior to data selection).
Fig. 4b. Mean signal (divided by the cosine of emission angle ε) measured by JIRAM spectrometer between PJ1 and PJ15 (black curve = mean signal in bins of 1° width, blue curve = standard deviation inside the same bins).
Comparison between the two panels demonstrates that uneven distribution in black curve of Fig. 4a is driven mostly by the filter imposed on signal. Planetocentric latitude is adopted.

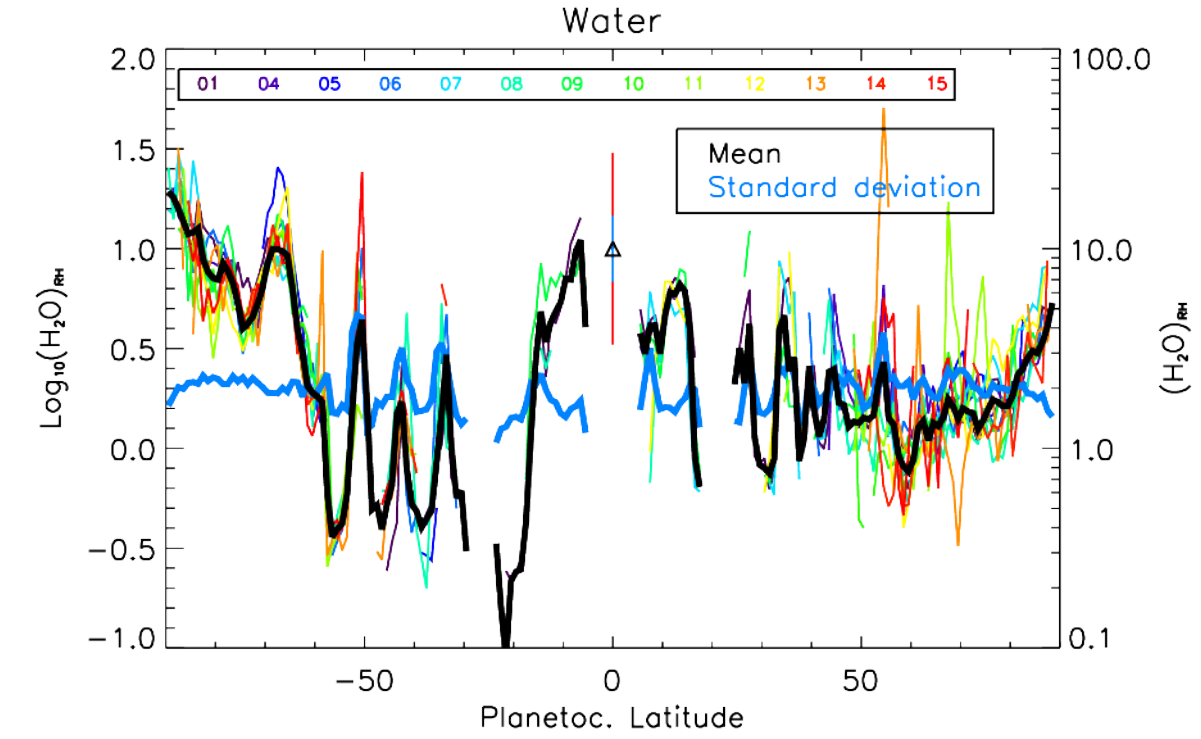
Water
01 04 05 06 07 08 09 10 11 12 13 14 15
Mean
Standard deviation
2.0
1.5
1.0
0.5
0.0
−0.5
−1.0
100.0
10.0
1.0
0.1
Log10(H2O)RH
(H2O)RH
−50
0
50
Planetoc. Latitude

Fig. 5a

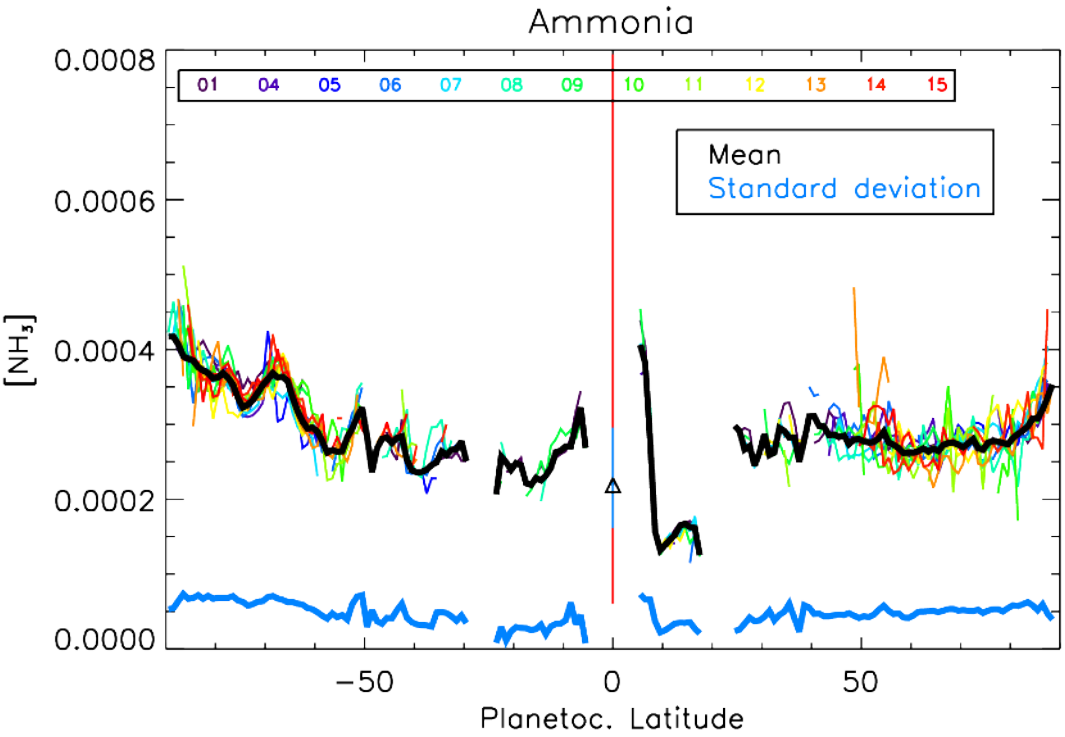
Ammonia
01 04 05 06 07 08 09 10 11 12 13 14 15
Mean
Standard deviation
0.0008
0.0006
0.0004
0.0002
0.0000
[NH3]
−50
0
50
Planetoc. Latitude

Fig. 5b

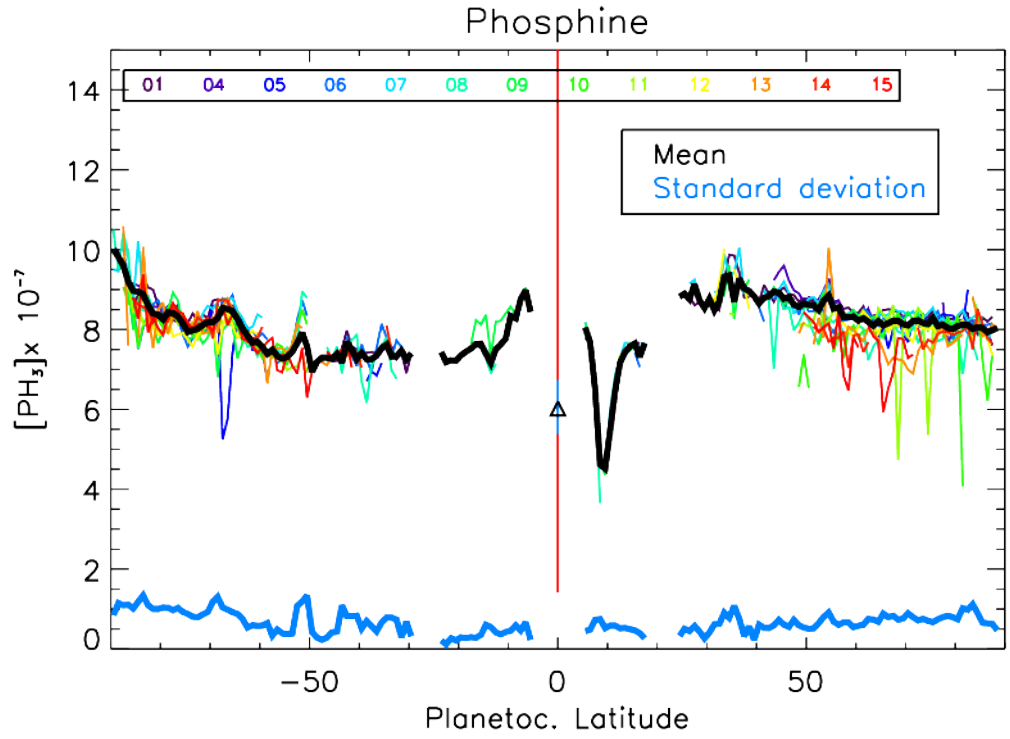
Phosphine
01 04 05 06 07 08 09 10 11 12 13 14 15
Mean
Standard deviation
[PH3]x 10-7
14
12
10
8
6
4
2
0
−50
0
50
Planetoc. Latitude

Fig. 5c

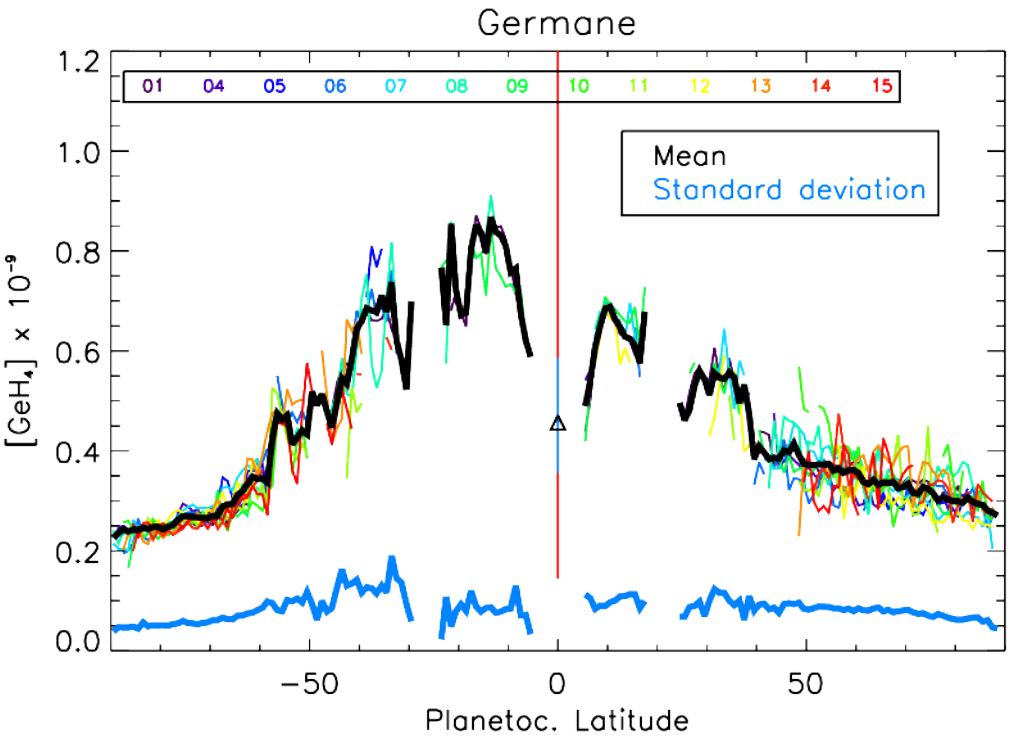
Germane
01 04 05 06 07 08 09 10 11 12 13 14 15
Mean
Standard deviation
[GeH4] x 10-9
1.2
1.0
0.8
0.6
0.4
0.2
0.0
−50
0
50
Planetoc. Latitude

Fig. 5d

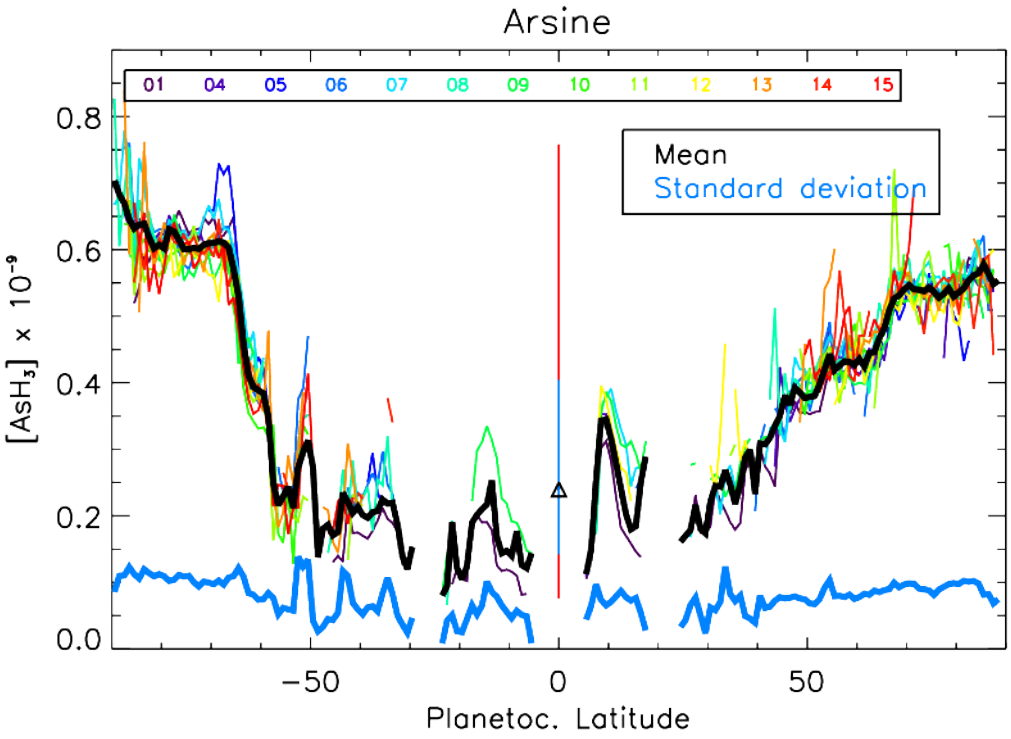

Fig. 5e

Figure 5. Abundance of minor gases in the troposphere (around 4.5 bars) of Jupiter's infrared-bright areas - as a function of latitude - retrieved from JIRAM spectrometer data.
Fig. 5a: water vapor relative humidity
Fig. 5b: ammonia volume mixing ratio
Fig. 5c: phosphine volume mixing ratio
Fig. 5d: germane volume mixing ratio
Fig. 5e: arsine volume mixing ratio
For each gas we present: thick black curve = mean value over the entire PJ1 – PJ15 population, thick blue curve = standard deviation over the entire PJ1 – PJ15 population, color thin curves = mean value over individual PJ (color key gives the PJ number). Latitude bin size is always 1°. Triangle at latitude 0° presents the a priori value for the gas abundance considered in the retrieval process. The red vertical bar at 0° presents the 1σ a priori uncertainty, the blue vertical bar the indicative 1σ a posteriori uncertainty. The latter is an effective figure for the retrieval uncertainty in the analysis of *individual* spectra.

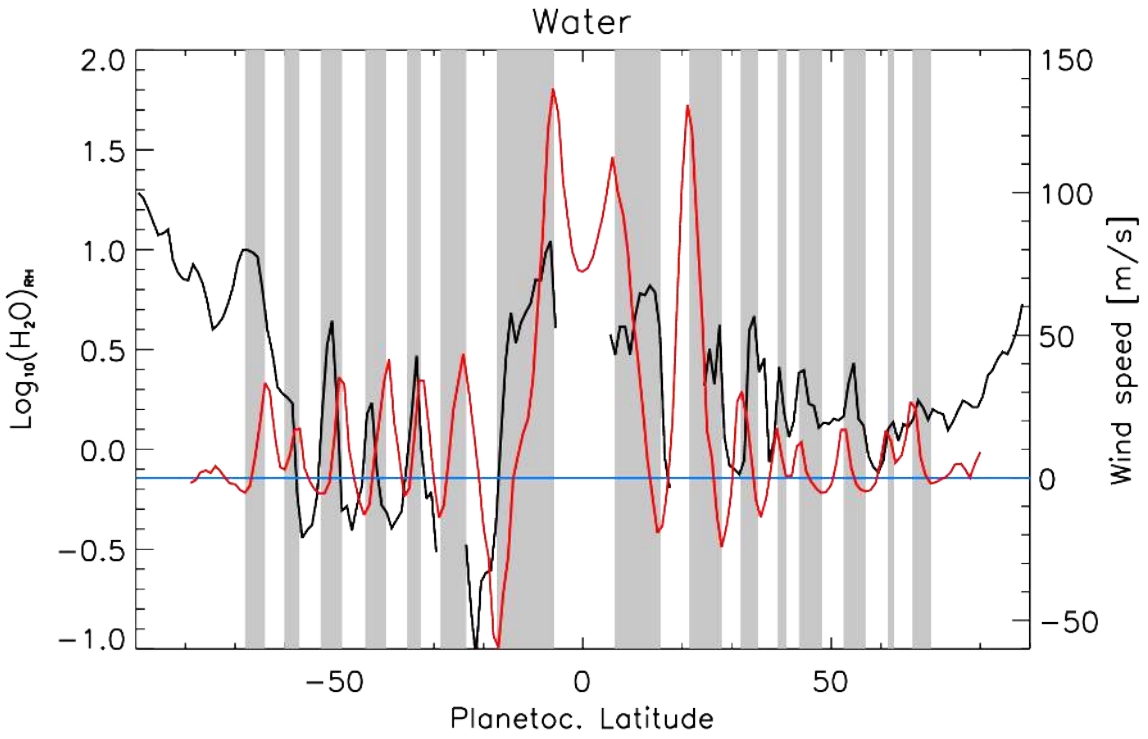

Fig. 6

Figure 6. Comparison of JIRAM-derived mean water vapour relative humidity (black curve) against zonal wind speeds (red curve) and belts positions as inferred in the visible range by Porco et al., [2003].

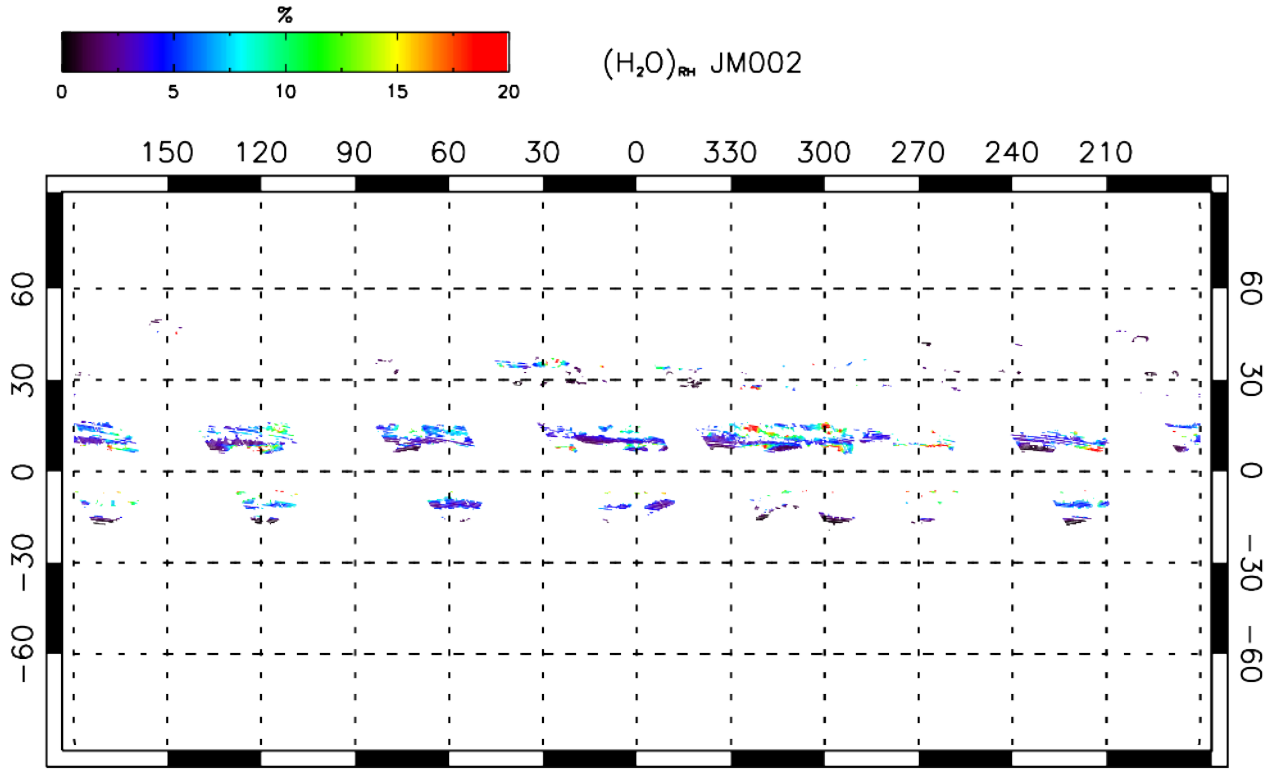
%
0
5
10
15
20
$(H_2O)_{RH}$ JM002
150
120
90
60
30
0
330
300
270
240
210
60
30
0
−30
−60

Fig. 7a

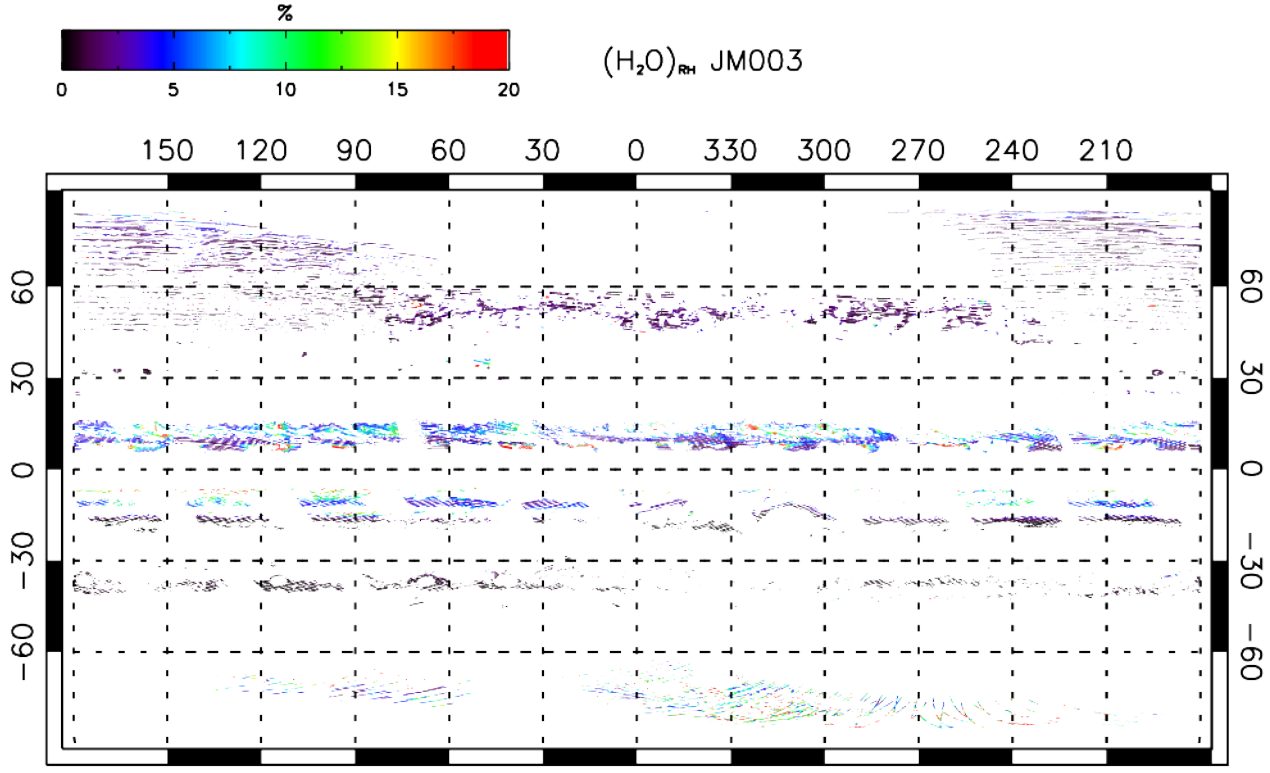
%
0
5
10
15
20
$(H_2O)_{RH}$ JM003
150
120
90
60
30
0
330
300
270
240
210
60
30
0
−30
−60

Fig. 7b

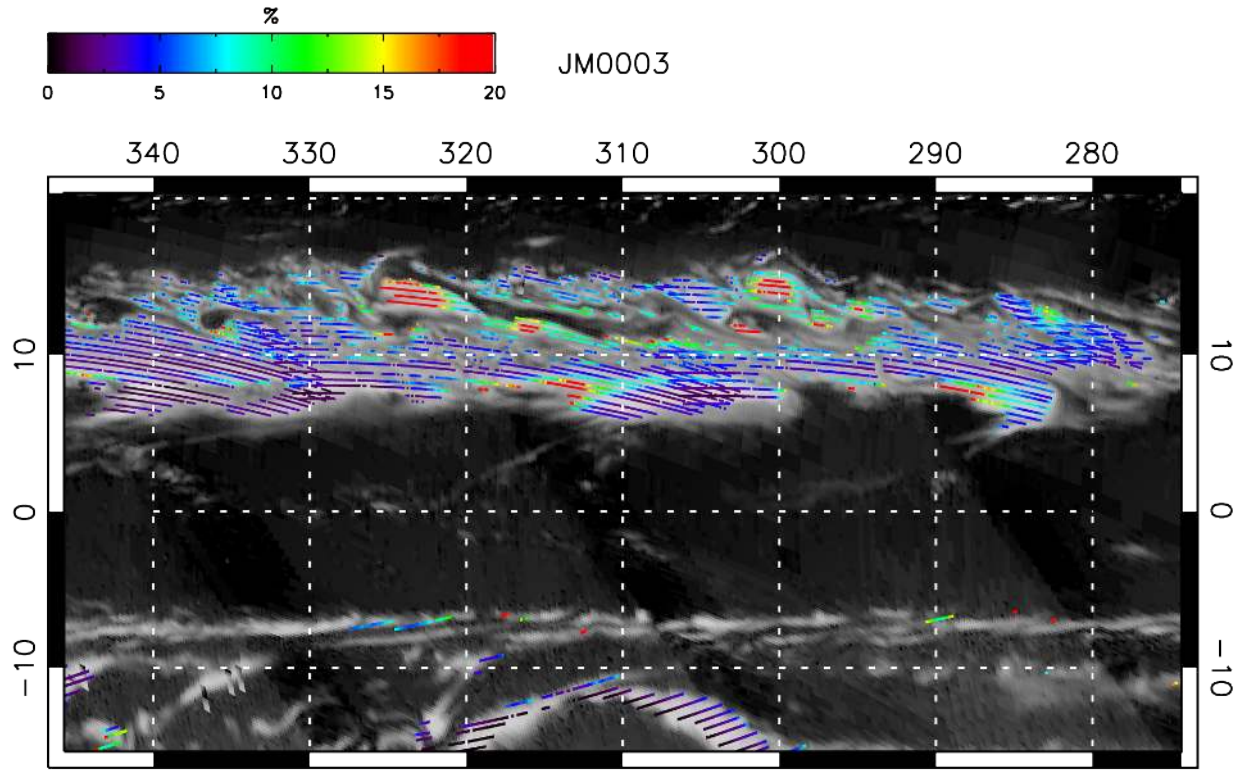

Fig. 7c

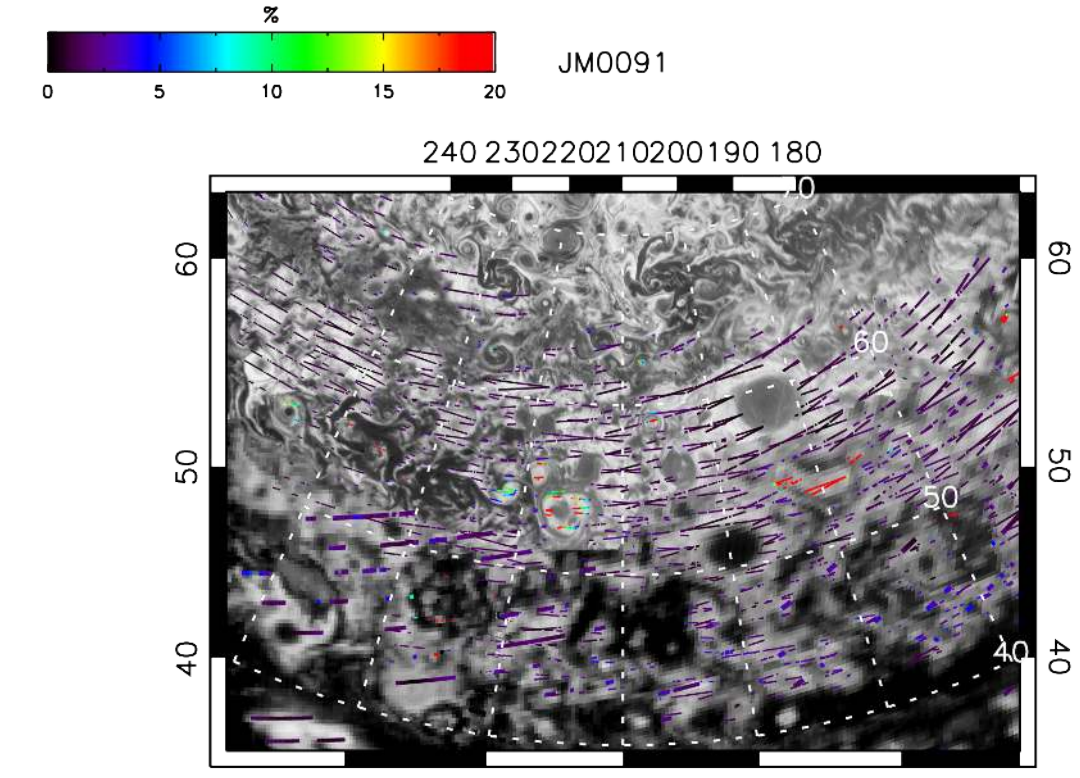

Fig. 7d

Figure 7. Examples of spatial distribution of water vapor relative humidity.
Fig. 7a. Global distribution from JIRAM spectrometer data acquired during planning period JM0002 (PJ1, see also fig. 1a)
Fig. 7b. As fig. 7a, for JM0003 (PJ1, see also fig. 1b)
Fig. 7c. Detail from JM0003
Fig. 7d. Detail from JM0091 - PJ9 (Oct. 24th, 2017)
For all maps, we adopt the System III longitudes - increasing westward - and planetocentric latitudes.
Background images in Fig. 7c and Fig. 7d are JIRAM M-filter (5 μm) mosaics, from frames acquired during the same perijove passage.

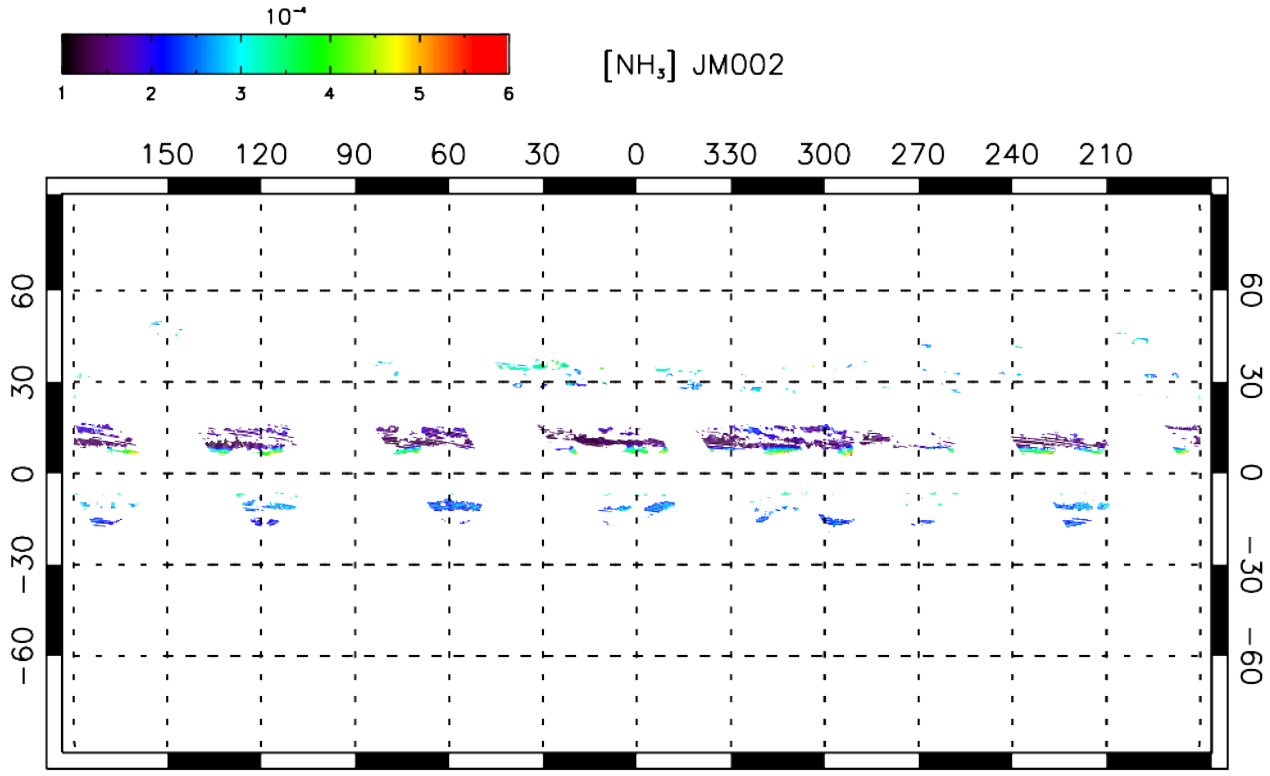
10⁻⁴
1
2
3
4
5
6
[NH₃] JM002
150
120
90
60
30
0
330
300
270
240
210
60
30
0
−30
−60

Fig. 8a

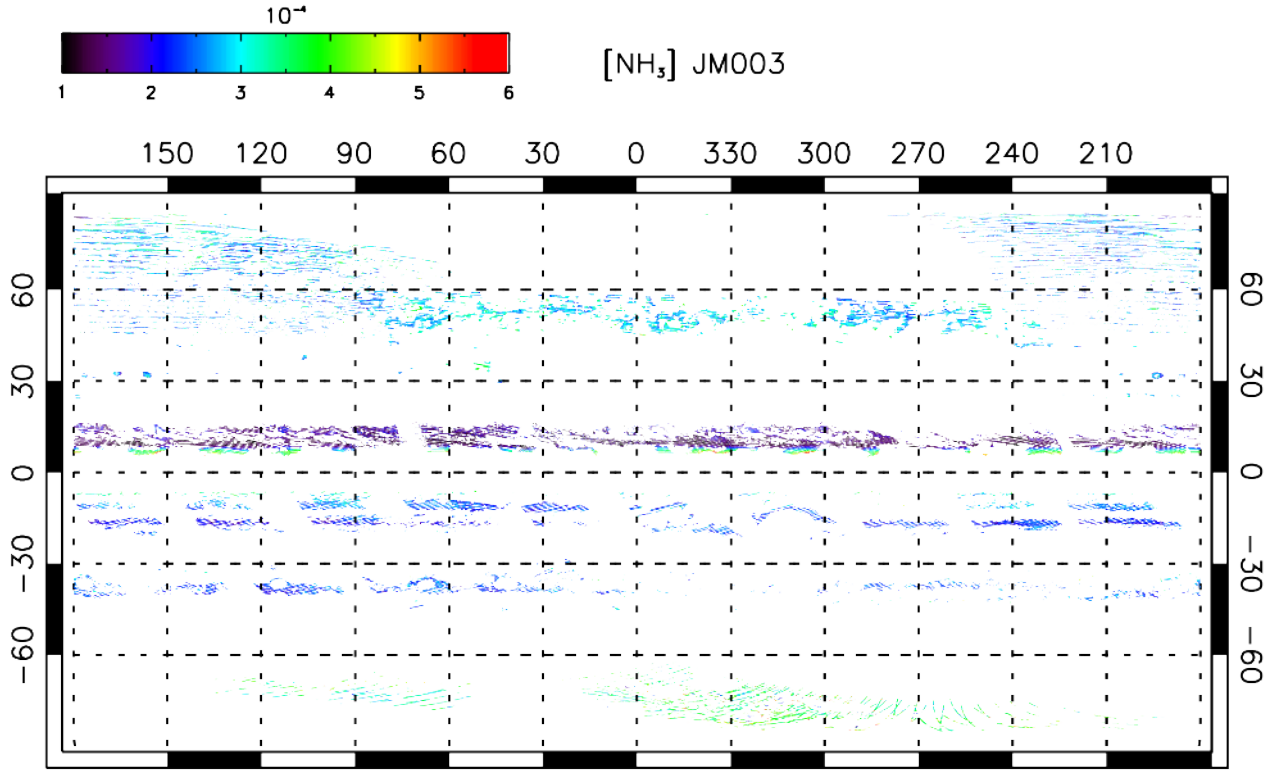
10⁻⁴
1
2
3
4
5
6
[NH₃] JM003
150
120
90
60
30
0
330
300
270
240
210
60
30
0
−30
−60

Fig. 8b

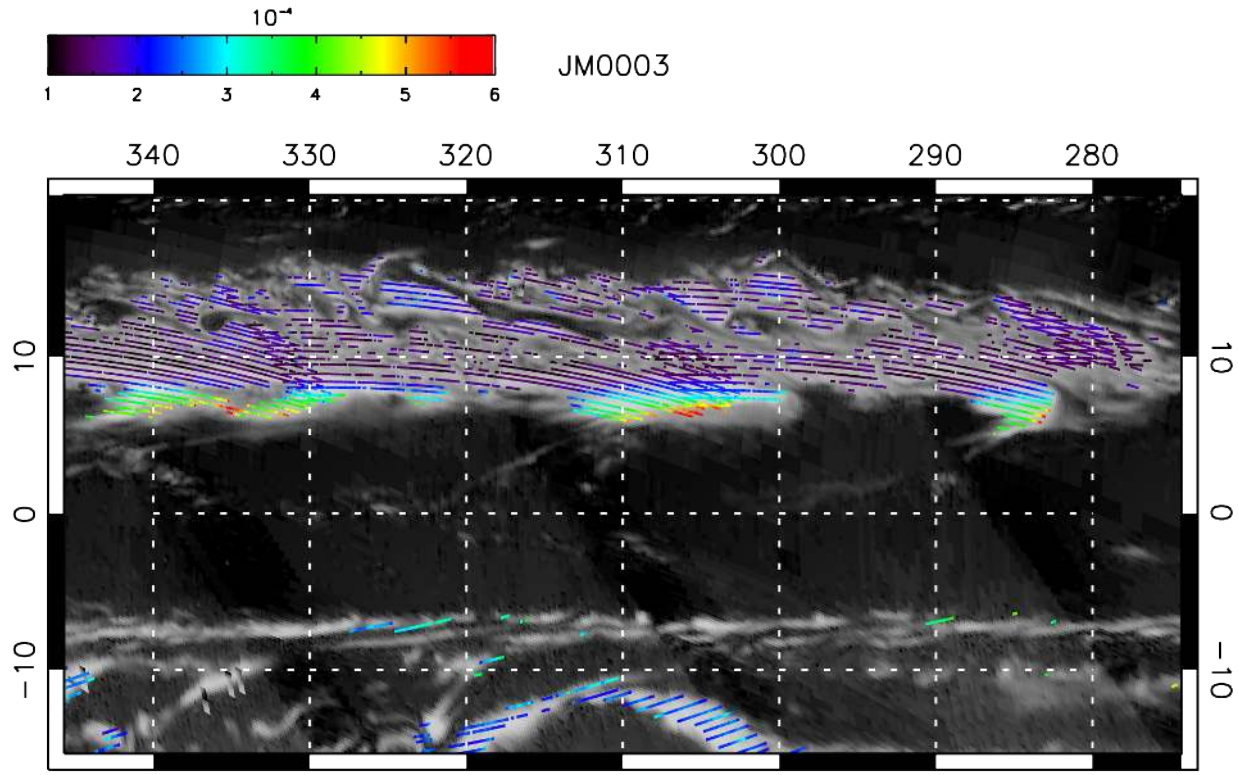

Fig. 8c

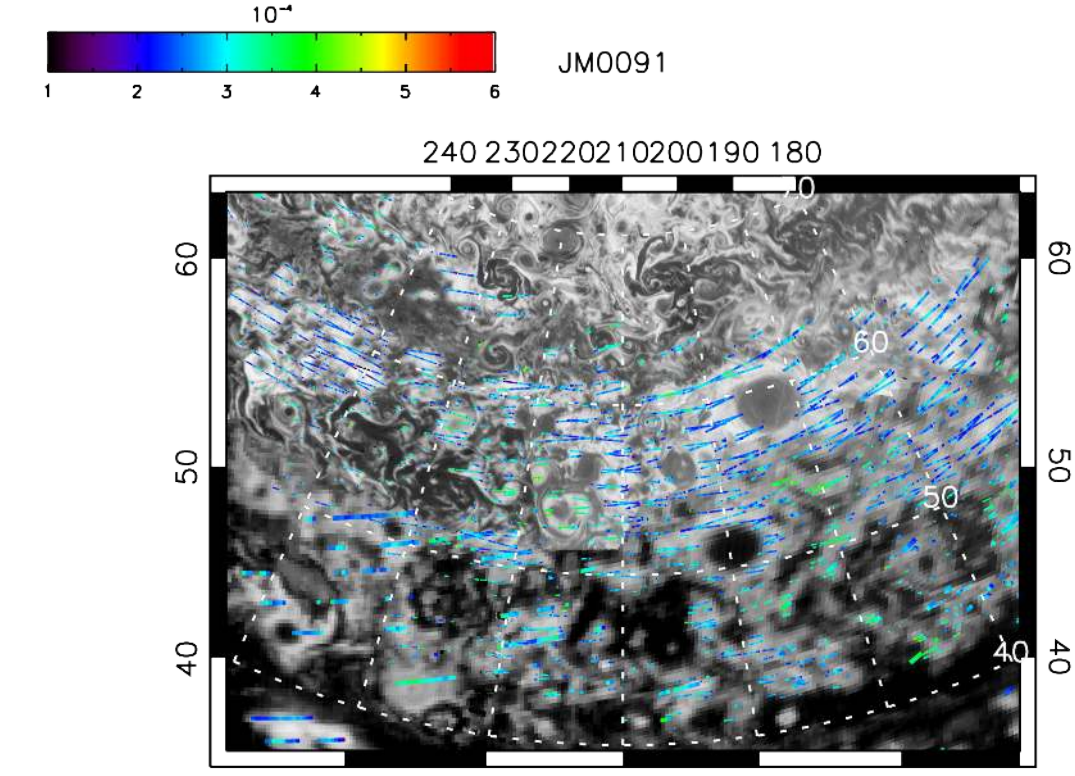

Fig. 8d

Figure 8. Examples of spatial distribution of ammonia volume mixing ratio.
Fig. 8a. Global distribution from JIRAM spectrometer data acquired during planning period JM0002 (PJ1, see also fig. 1a)
Fig. 8b. As fig. 8a, for JM0003 (PJ1, see also fig. 1b)
Fig. 8c. Detail from JM0003
Fig. 8d. Detail from JM0091 - PJ9 (Oct. 24th, 2017)
For all maps, we adopt the System III longitudes - increasing westward - and planetocentric latitudes.
Background images in Fig. 8c and Fig. 8d are JIRAM M-filter (5 μm) mosaics, from frames acquired during the same perijove passage.

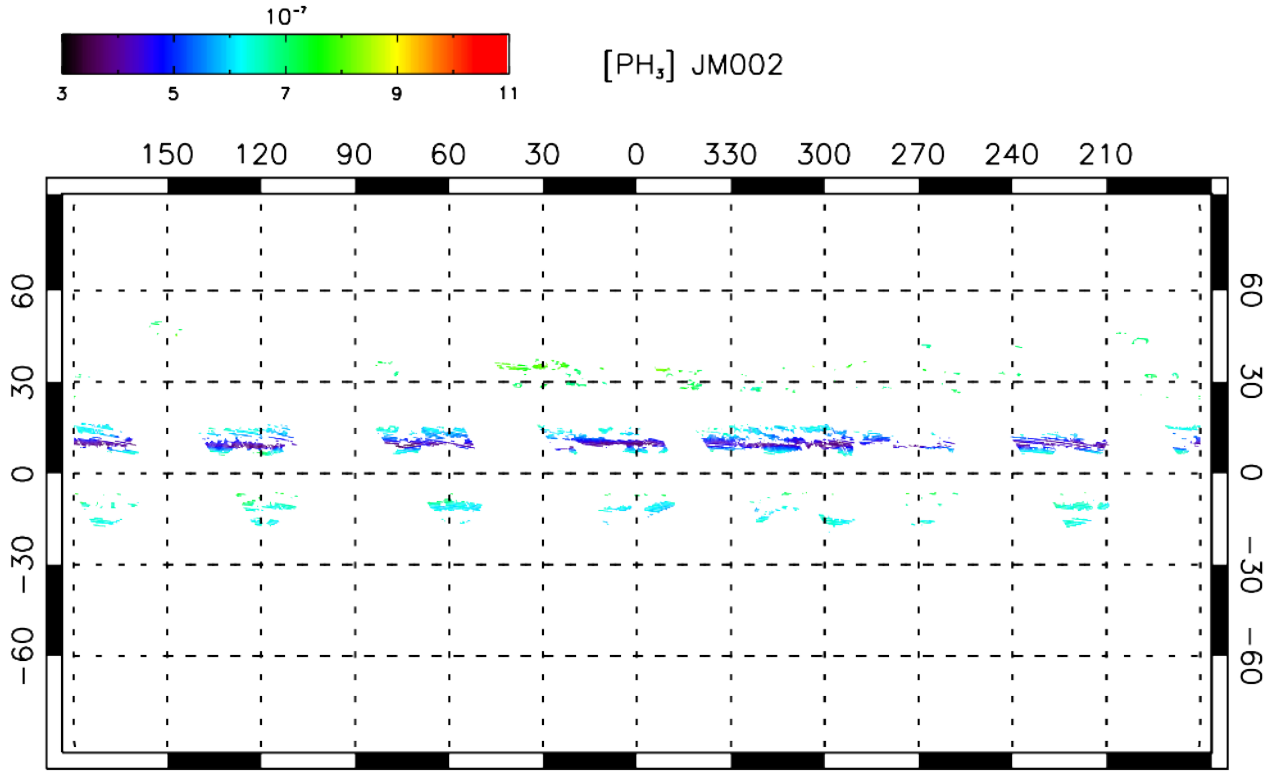

Fig. 9a

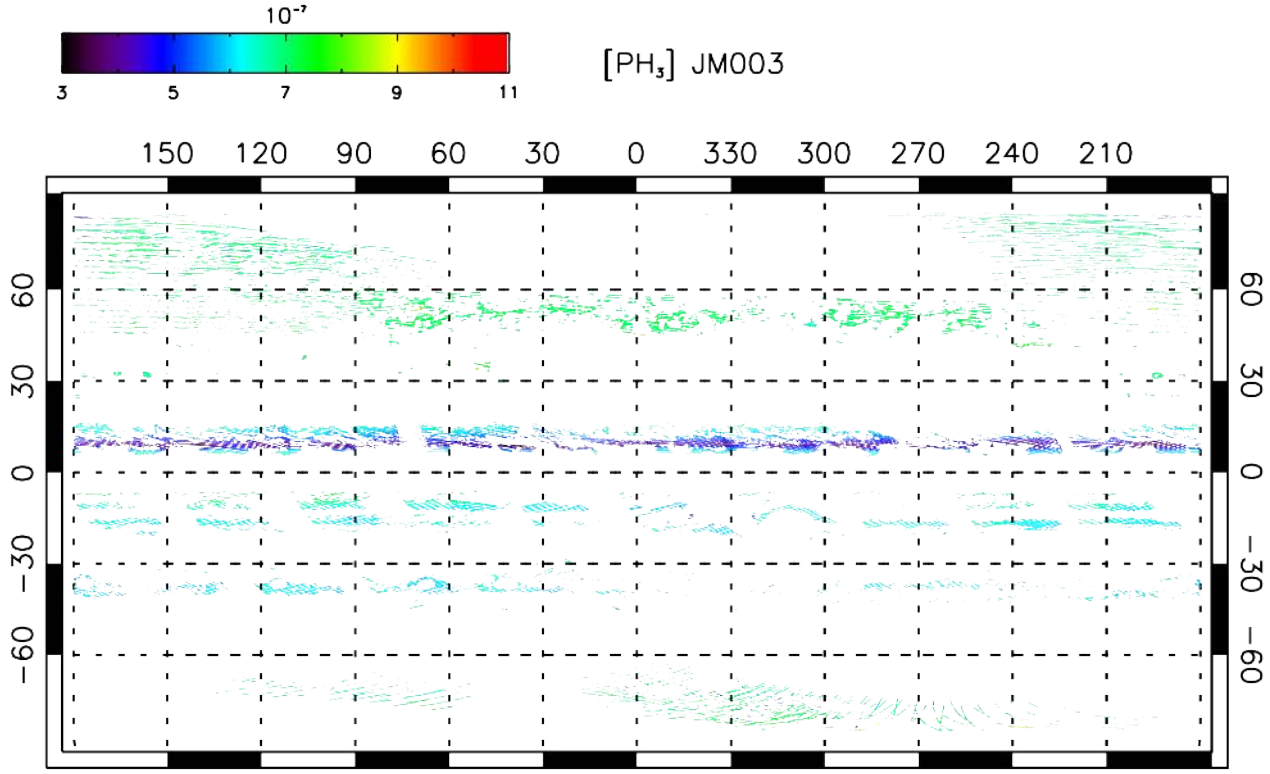

Fig. 9b

Figure 9. Examples of spatial distribution of phosphine volume mixing ratio.
Fig. 9a. Global distribution from JIRAM spectrometer data acquired during planning period JM0002 (PJ1, see also fig. 1a)
Fig. 9b. As fig. 9a, for JM0003 (PJ1, see also fig. 1b)
For both maps, we adopt the System III longitudes - increasing westward - and planetocentric latitudes.

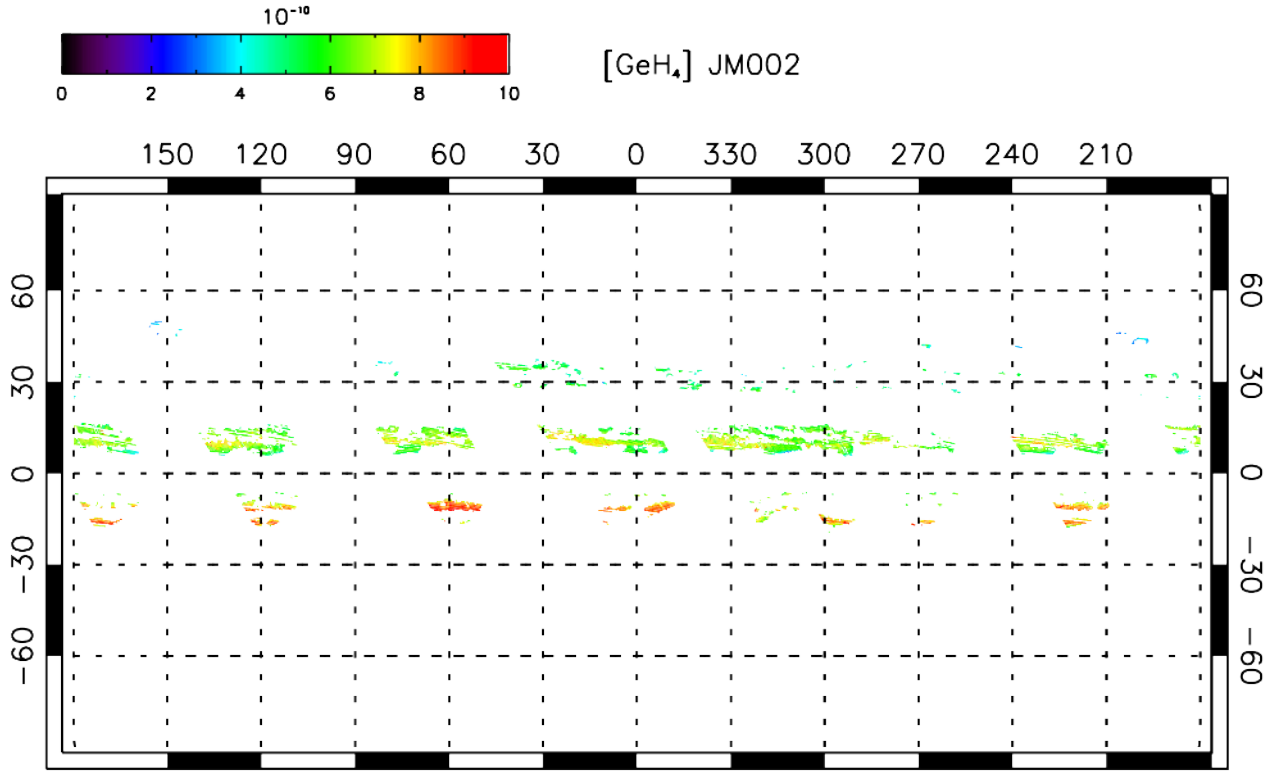

Fig. 10a

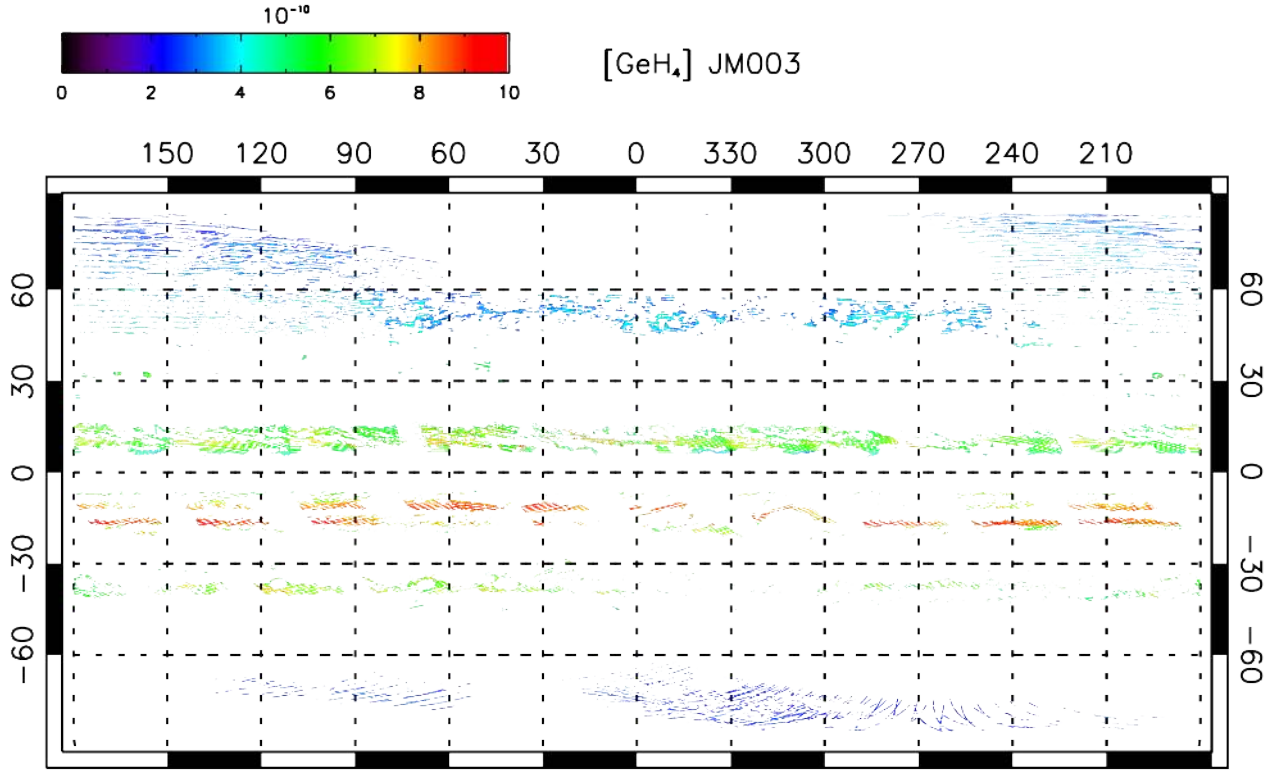

Fig. 10b

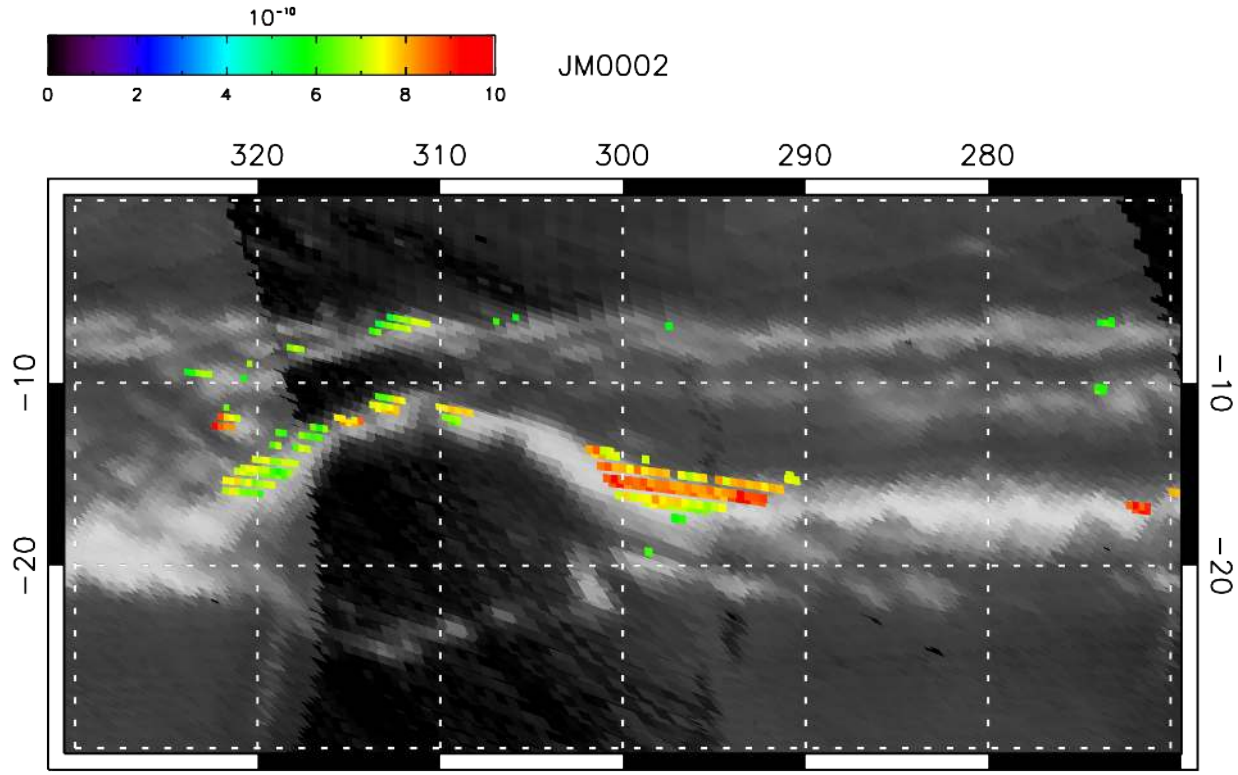

Fig. 10c

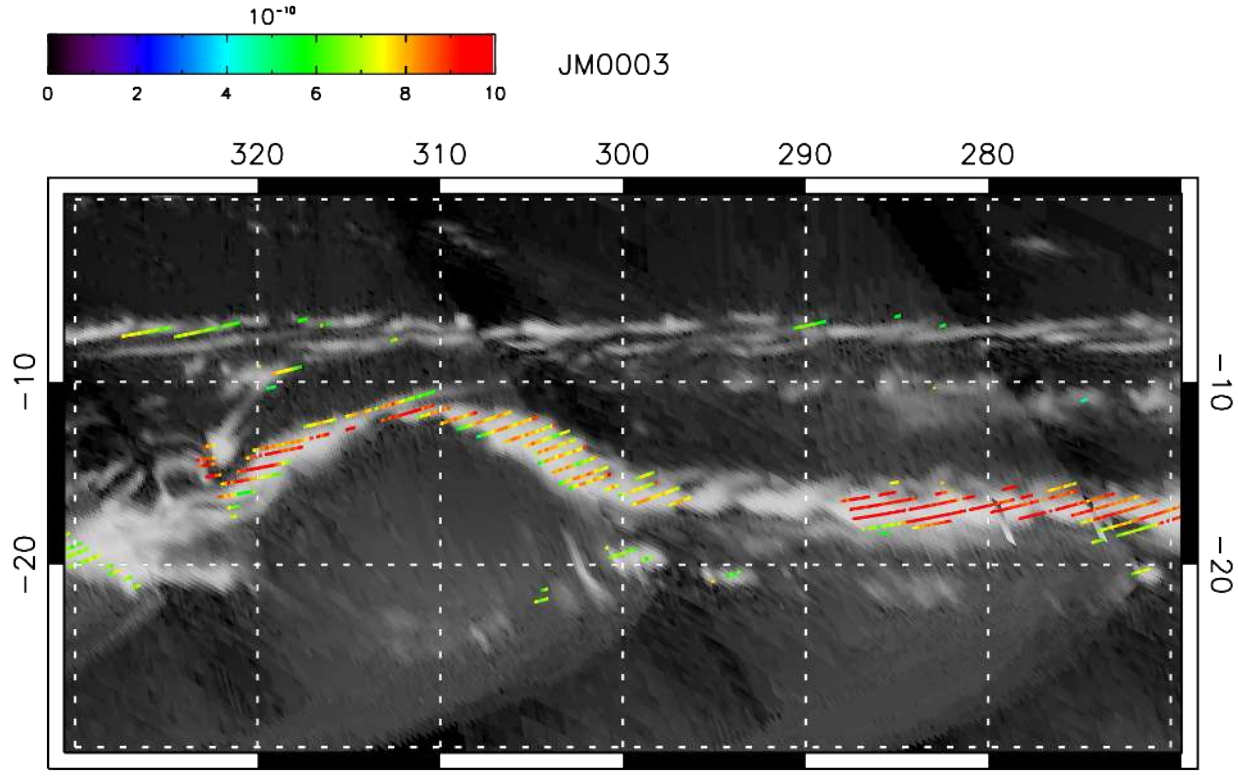

Fig. 10d

Figure 10. Examples of spatial distribution of germane volume mixing ratio.
Fig. 10a. Global distribution from JIRAM spectrometer data acquired during planning period JM0002 (PJ1, see also fig. 1a)
Fig. 10b. As fig. 10a, for JM0003 (PJ1, see also fig. 1b)
Fig. 10c. Detail from JM0002
Fig. 10d. Detail from JM0003
For all maps, we adopt the System III longitudes - increasing westward - and planetocentric latitudes.
Background images in Fig. 10c and Fig. 10d are JIRAM M-filter (5 μm) mosaics, from frames acquired during the same perijove passage.

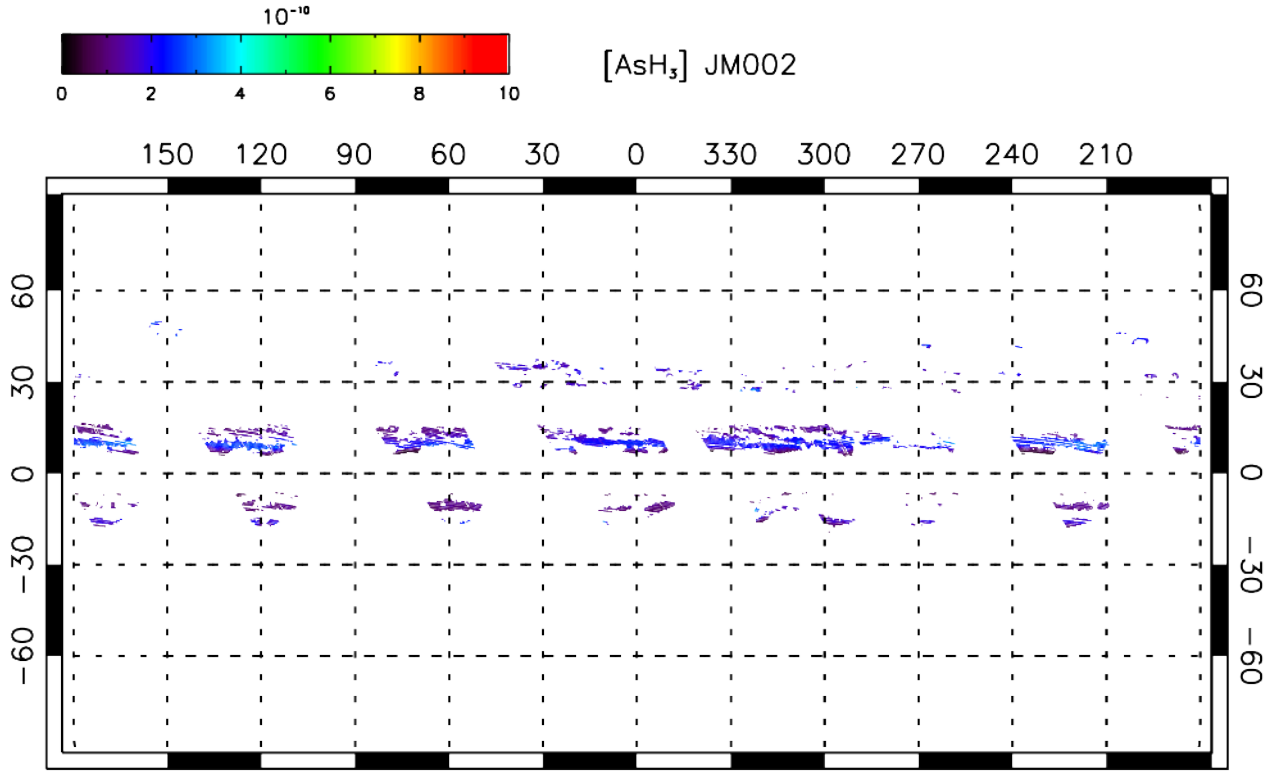

Fig. 11a

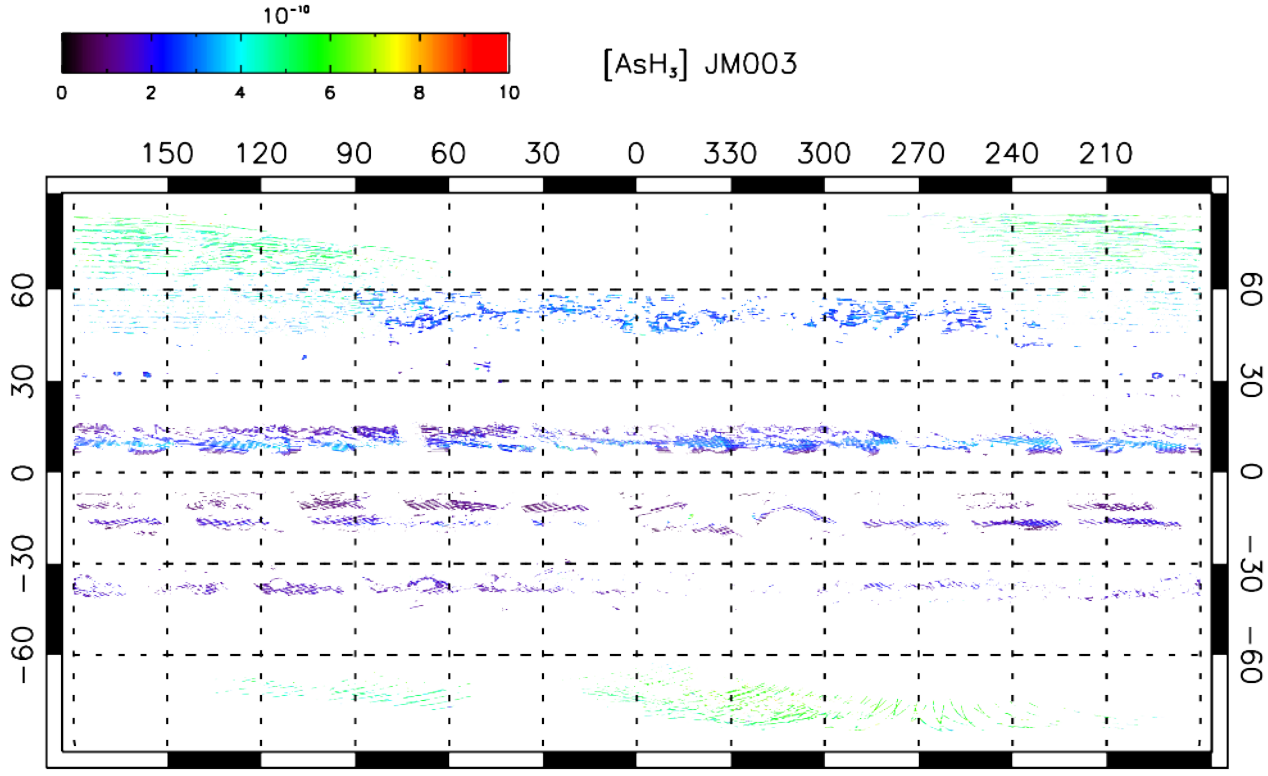

Fig. 11b

Figure 11. Examples of spatial distribution of arsine volume mixing ratio.
Fig. 11a. Global distribution from JIRAM spectrometer data acquired during planning period JM0002 (PJ1, see also fig. 1a)
Fig. 11b. As fig. 10a, for JM0003 (PJ1, see also fig. 1b)
For both maps, we adopt the System III longitudes - increasing westward - and planetocentric latitudes.

D

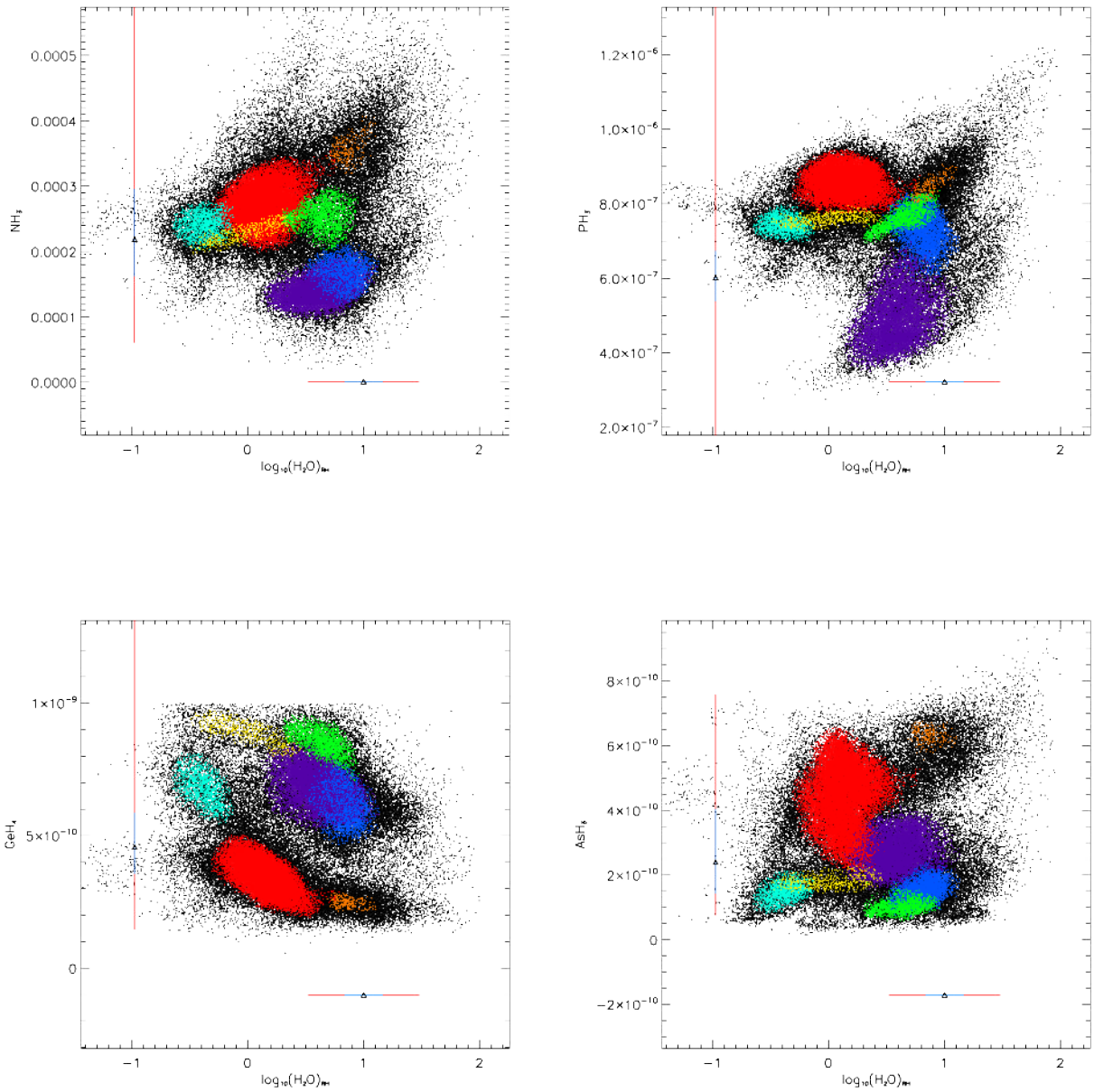
0.0005
0.0004
0.0003
0.0002
0.0001
0.0000
NH3
−1
0
1
2
log10(H2O)ice
1.2×10−6
1.0×10−6
8.0×10−7
6.0×10−7
4.0×10−7
2.0×10−7
PH3
1×10−9
5×10−10
0
GeH4
8×10−10
6×10−10
4×10−10
2×10−10
0
−2×10−10
AsH3

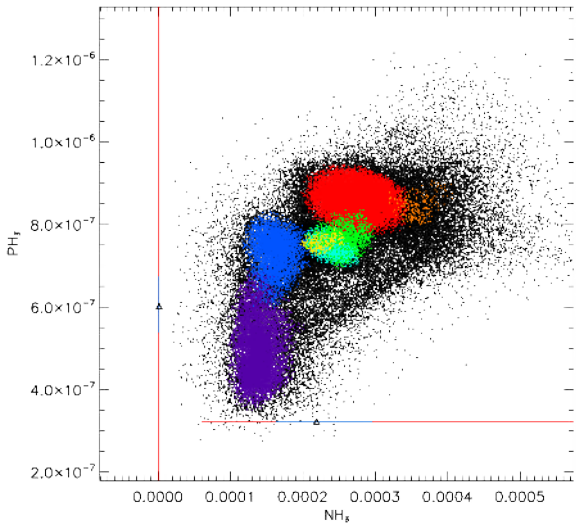
1.2×10⁻⁶
1.0×10⁻⁶
8.0×10⁻⁷
6.0×10⁻⁷
4.0×10⁻⁷
2.0×10⁻⁷
PH₃
0.0000
0.0001
0.0002
0.0003
0.0004
0.0005
NH₃

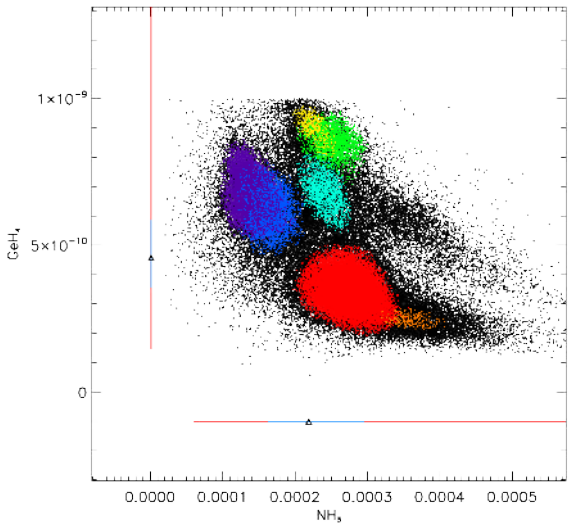
1×10⁻⁹
5×10⁻¹⁰
0
GeH₄
0.0000
0.0001
0.0002
0.0003
0.0004
0.0005
NH₃

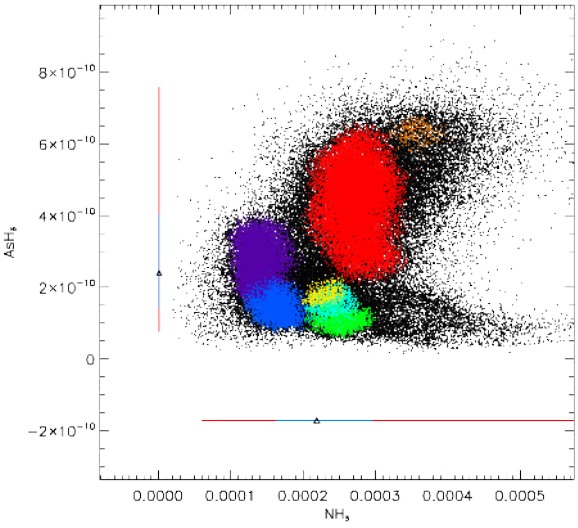
8×10⁻¹⁰
6×10⁻¹⁰
4×10⁻¹⁰
2×10⁻¹⁰
0
−2×10⁻¹⁰
AsH₃
0.0000
0.0001
0.0002
0.0003
0.0004
0.0005
NH₃

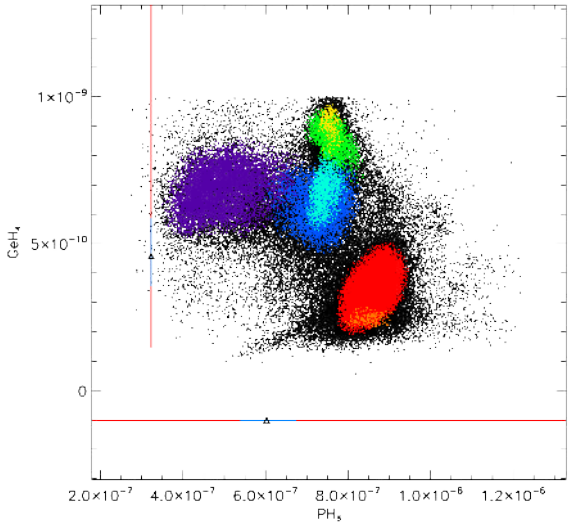
1×10⁻⁹
5×10⁻¹⁰
0
GeH₄
2.0×10⁻⁷
4.0×10⁻⁷
6.0×10⁻⁷
8.0×10⁻⁷
1.0×10⁻⁶
1.2×10⁻⁶
PH₃

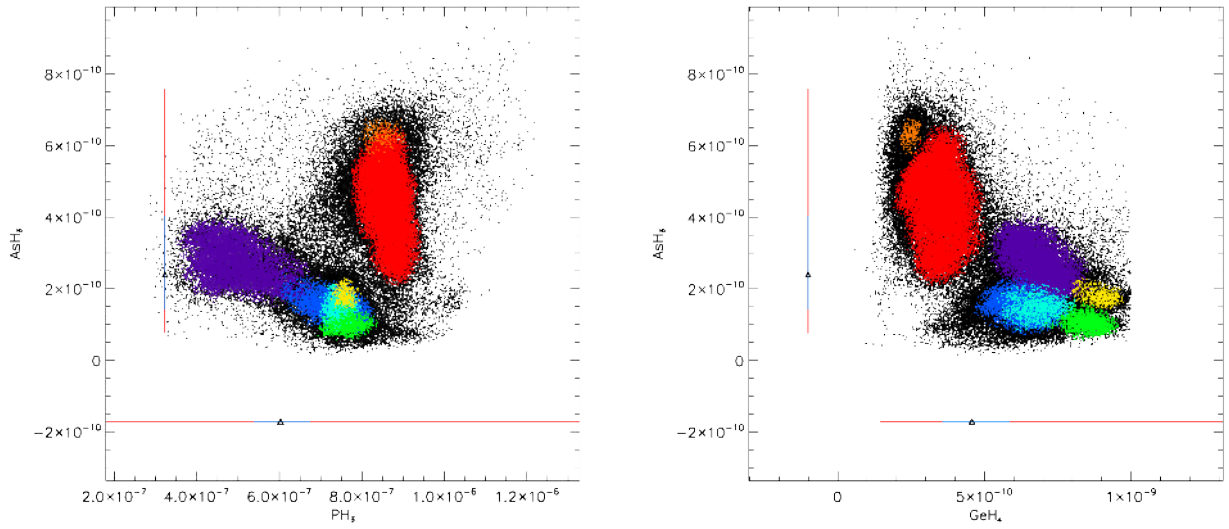

Figure 12. Distribution of JIRAM measurements from PJ1 as a function of the retrieved contents of different minor gases. A scatter plot is presented for each possible pair of gases. Each point represents the retrieved values from a single spectrum and each scatter plot contains all spectra from PJ1. Points in color represent members of the different clusters (regions of higher point density) identified by the HDBSCAN algorithm. Black points represent the spectra not assigned to any cluster.
Triangles presents the a priori (and initial) values for the gas abundances considered in the retrieval process. The red bars present the 1σ a priori uncertainties, the blue vertical bars the approximate (conservative) 1σ a posteriori uncertainties.

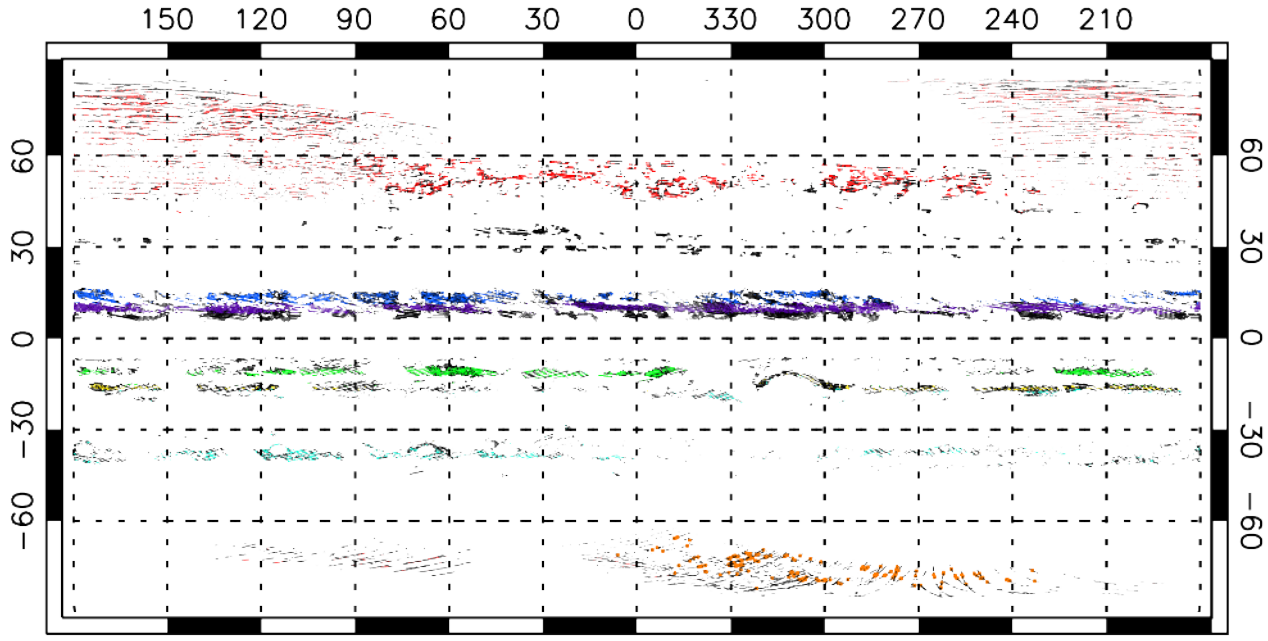

Fig. 13

Figure 13. Spatial distributions of the populations of different cluster presented in Fig. 12. Cluster 6 elements (orange) are marked by the “+” sign, to improve visibility.